University of Alberta

The Application of Electrospun Photocatalytic $BiFeO_3$ Nanofibers in Water Treatment

by

Parmiss Mojir Shaibani

A thesis submitted to the Faculty of Graduate Studies and Research
in partial fulfillment of the requirements for the degree of

Master of Science

in

Materials Engineering

Department of Chemical and Materials Engineering

Fall 2012

Edmonton, Alberta

Dedication

I would like to dedicate this thesis to my wonderful family who supported me unconditionally and especially to my caring husband without whom this work could not have been completed.

Abstract

One-dimensional $BiFeO_3$ (BFO) nanofibers were fabricated using the simple electrospinning of a Nylon6/BFO solution, carried out on a homemade electrospinning apparatus, and subsequent calcination at 600 °C. The photocatalytic activity of the nanofibers and their application in water purification was investigated against 4-Chlorophenol (4CP) as a model water contaminant. A pseudo-first order kinetics model was utilized in order to understand the degradation kinetics of the system. The SEM images of the as-spun samples demonstrated the successful production of nanofibers and the SEM images of the samples after calcination confirmed the integrity of the continuous BFO nanofibers. XRD analysis indicated the dominant presence of BFO phase throughout the calcinated nanofibers. The results of the UV-Vis spectroscopy exhibit the degradation of the 4CP by means of the Photocatalytic activity of the BFO nanofibers. The kinetics of the photodegradation of 4CP is believed to be governed by a pseudo-first order kinetics model.

Acknowledgement

Many individuals have helped me over the period of my graduate studies as a master student and here I am given a chance to briefly express my humble gratitude for all that they have done.

First, I would like to thank my esteemed supervisor, Prof. Thomas Thundat for believing in me and providing me with the opportunity to excel academically by allowing me to use of his facilities as well as guiding me in my experience as a master student with his vast knowledge and years of highly awarded research record. This work could not have been conducted without his leadership and insight.

I would also like to express my gratitude towards Dr. Prashanti Kovur for providing me with advice on the preparation of BFO nanofibers, their characterization and application in water treatment and her overall helpfulness and considerate guidance throughout this research.

Next, I would like to thank Prof. T.S. Natarajan and Mr. David Hedden for helping design and set up the electrospinning system. In addition, I would like to show my appreciation to all the members of our research group for their help in various stages of my research.

I am also deeply grateful to the Nano Fabrication Lab, Alberta Centre for Surface Engineering & Sciences (ACSES) and Oil Sands and Coal Interfacial Engineering Facility (OSCIEF) for characterization experiments.

I want to acknowledge Canada Excellence Research Chairs (CERC) program and the faculty of Chemical and Materials Engineering at University of Alberta as well for providing financial support during the length of my master's program.

Last, but certainly not least, I would like to thank my supportive family and friends for their care and support and especially my dear husband Amirreza Sohrabi for his help every step of the way from the beginning and his caring nature for accompanying me through the highs and lows of this project.

Table of contents

List of tables

List of figures

List of abbreviations

°C	Degree centigrade
2CP	2-chlorophenol
4CP	4-Chlorophenol
Å	Angstrom
Ac	Alternating current
Ag	Silver
Al_2O_3	Aluminum oxide
AOP	Advanced oxidation processes
BFO	Bismuth ferrite
Bi	Bismuth
C	Concentration
Ca	Calcium
CBZ	Carbamazepine
Cd	Cadmium
cm	Centimeter
CO_2	Carbon dioxide
CR	Congo red
Cr	Chromium
Dc	Direct current
DMF	Dimethylformamide
DNA	Deoxyribonucleic acid
DOC	Dissolved organic carbon
DS	Dissolved solids
e^-	Electron
E. coli	Escherichia coli
Eq.	Equation
et al.	And others
eV	Electron volt
Fe	Iron
FESEM	Field emission electron microscopy
Fig	Figure
g/mol	Grams per mole
$GaFeO_3$	Gallium ferrite
H	Hydrogen
h^+	Hole
H_2O	Water
H_2O_2	Hydrogen peroxide
hr	Hour
i.e.	Id est
K	Potassium

k	Degree kelvin
k	React rate constant
kDa	Kilo Dalton
kV	Kilovolt
ln	Natural logarithm
$LuFe_2O_4$	Lutetium ferrite
mA	Milliamp
MC-LR	Microcystin-LR
Mg	Magnesium
mg	Milligram
min	Minute
ml	Milliliter
ml/hr	Milliliters per hour
mm	Millimeter
MW	Molecular weight
Ni	Nickel
nm	Nanometer
NOM	Natural organic matter
O_2	Oxygen
Pb	Lead
PEO	Poly (ethylene oxide)
PGA	Poly (glycolic acid)
PLA	Poly (lactic acid)
PLGA	Poly (lactide-co-glycolide)
PLLA	Poly-L-lactic acid
Pt	Platinum
R^2	Coefficient of determination
rpm	Revolutions per minute
SEM	Scanning electron microscopy
Si	Silicium
SiO_2	Silica
Sn	Tin
SnO_2	Tin dioxide
t	Time
$TbMnO_3$	Terbium manganese oxide
Ti	Titanium
TiO_2	Titanium oxide
TNP	Titanium oxide nanoparticles
TSC	Titanium oxide solution combustion
UV-Vis spectroscopy	Ultraviolet- Visible spectroscopy

UVC	Ultra Violet C
W	Watt
w/v	Weight per volume
XRD	X-ray diffraction
Zn	Zinc
ZnO	Zinc oxide
µg	Microgram
µl	Microliter
µm	Micron

Chapter 1: Introduction

In this chapter, a general introduction is given on the concepts explored in the current work. The electrospinning process and some of its well-known applications are explained. Different water treatment methods are introduced and finally the material used in this research is briefly described.

1.1. Electrospinning

Electrospinning, also known as electrostatic spinning, is a process in which a high voltage is applied to a polymeric solution to fabricate cylindrical electrospun fibers of micron or sub-micron diameter (nanofibers). The process involves the usage of a high voltage power supply, an electrically conductive nozzle carrying a polymeric solution, to which the high voltage is applied and an electrically conductive collector (target) which is grounded. The invention of electrospinning dates back to May 1900 when J. F. Cooley patented the technique [1] as well as February 1902 [2], followed by a patent from July 1902 filed by W. J. Morton [3]. The observation of electrospraying however was initially recorded in the 16th century when William Gilbert witnessed that as a droplet of water was approached by an electrically charged piece of amber, the droplet would form a cone shape and smaller droplets would fly form the very tip of the cone [4].

The method of electrospinning continued to improve through time with the reports of manufacturing artificial silk surfacing in 1929 and a patent on the electrospinning of plastics in 1934 by Anton Formhals. Even though attempts had

been made to make electrospinning commercially recognized, the application of electrospun in filtration as a part of the nonwovens industry was the first successful record for the commercialization of this technique [5].

The interest in electrospinning was revived in the 1990s by reports from Reneker et al. exploring the electrospinning process and its applications [5,6]. Since then diverse applications have been found for nanofibers, which will be further described in Section 1.3.

1.2. Electrospinning process and types

As mentioned above, electrospinning comprises of the application of a high voltage to a polymeric solution with a specific flow rate through a nozzle (also called a spinneret) to produce fibers with a diameter size in the range of micrometers to nanometers. A schematic of a typical electrospinning setup is illustrated in Fig.1.1.a; Fig.1.1.b shows an SEM image of common electrospun fibers. The process begins as the voltage is applied to the solution droplet formed at the tip of the nozzle and the droplet is transformed into a cone. This cone, known as the Taylor cone, is formed as a result of the competition between the electrostatic forces applied to the droplet and the surface tension of the droplet.

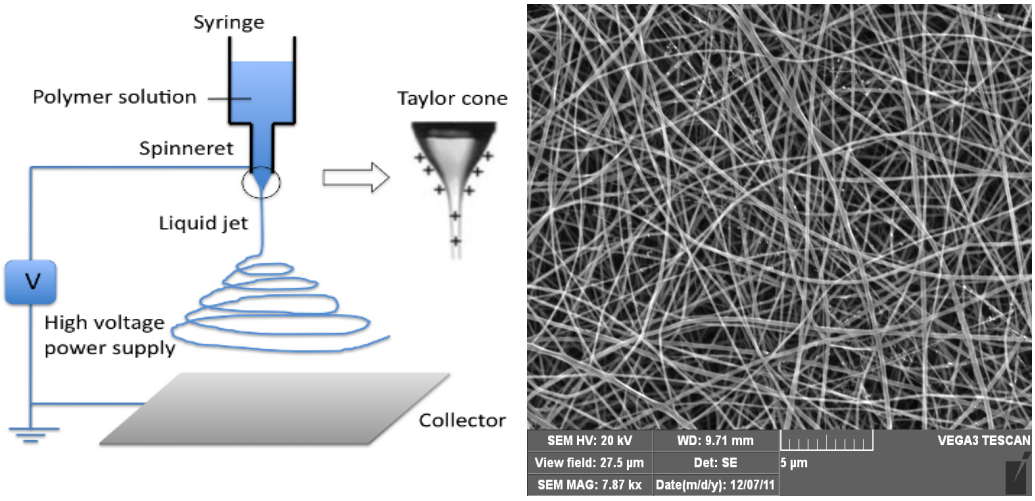

a b

Figure 1.1.a. Schematic of a typical electrospinning setup [10], b. SEM image of electrospun nanofibers; the scale represents 5 µm.

Taylor first described the phenomena surrounding the formation of this cone and the forces acting upon the protrusion resulting in the deformation of the droplet in 1964 [7-9]. If the voltage is high enough, the electrostatic forces will overcome the surface tension of the Taylor cone thus forming a continuous charged polymeric jet. Subsequently, the jet flies towards the grounded target to complete the electrospinning procedure. The gradual formation of the jet as voltage is increased to a threshold amount can be seen in Fig.1.2.

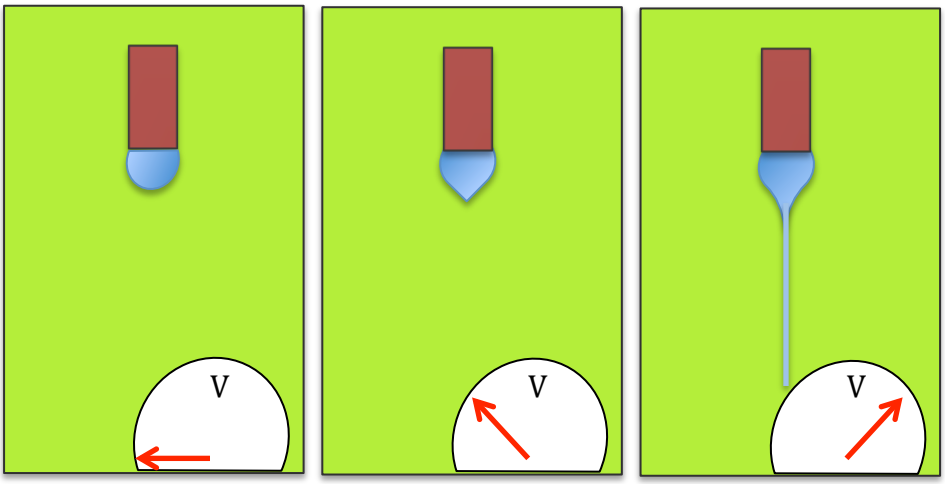

Figure 1.2.a. The droplet at the tip of the nozzle with no applied voltage, b. Taylor cone formed by applying high voltage but not high enough to overcome surface tension, c. Polymeric jet formed as a result of a voltage higher than the threshold required to exceed the surface tension.

Electrospinning is conducted in different manners. The most general division of electrospinning types is into horizontal and vertical electrospinning. Since there are virtually no differences between the two types due to the fact that gravity forces are negligible compared to the electrostatic forces and the mass of the polymer jet, both vertical and horizontal systems are used to produce electrospun nanofibers.

A recently established type of electrospinning is co-axial electrospinning, which utilizes a number of needles with different diameters inside each other containing different solutions to produce core-shell fibers. This configuration of nozzles is often referred to as a co-axial spinneret. One of the advantages of performing co-axial electrospinning is enabling the incorporation of materials that cannot be

electrospun in the conventional way, inside spinnable polymers acting as the fiber shell. Numerous accounts of the fabrication of core-shell fibers have been reported for a variety of applications [10-14]. Fig.1.3.a demonstrates a co-axial spinneret used in an electrospinning setup and Fig1.3.b and Fig.1.3.c illustrate SEM and TEM images of the produced core-shell fibers, respectively. It should be

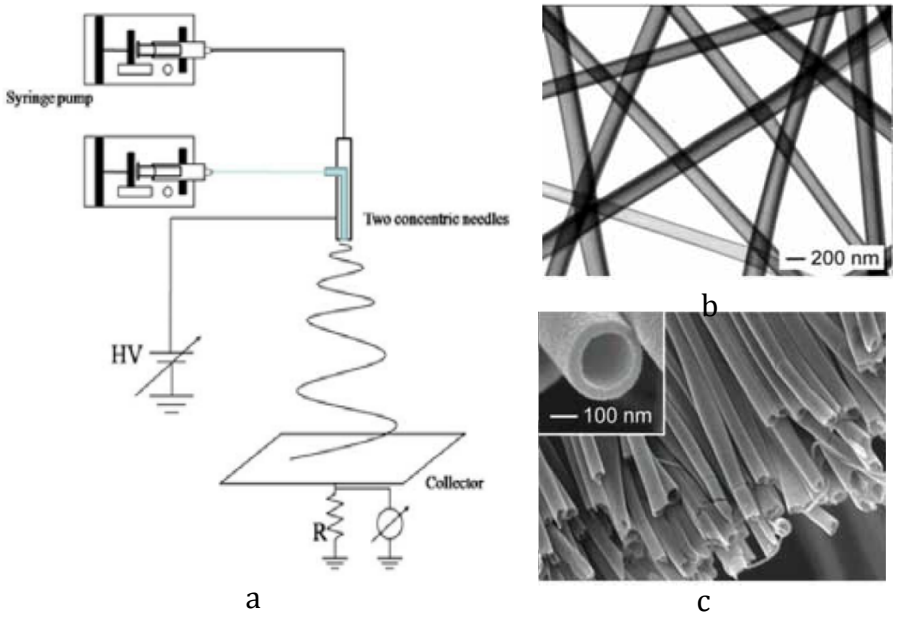

Figure 1.3.a. Schematic of a co-axial electrospinning configuration [15], b. TEM image of core-shell fibers [10], c. SEM image of core-shell fibers [10].

mentioned that co-axial electrospinning also enables the fabrication of hollow fibers to increase the surface area of the fibers.

Another form of electrospinning is conducted using different structures acting as the grounded collector. The aim of this is to achieve aligned fibers and the most common collector used to obtain aligned fibers is a rotating drum. The drum is usually connected to a motor at a specific speed, which ensures the formation of unidirectional electrospun fibers. Another effective method to align the fibers is

the usage of parallel metallic plates as the target; examples of deploying this type of target can be found in studies by Kong et al. [16] and Cooper et al. [17]. Representations of electrospinning setups for fiber alignment as well as SEM images of successfully spun aligned fibers can be seen in Fig.1.4.

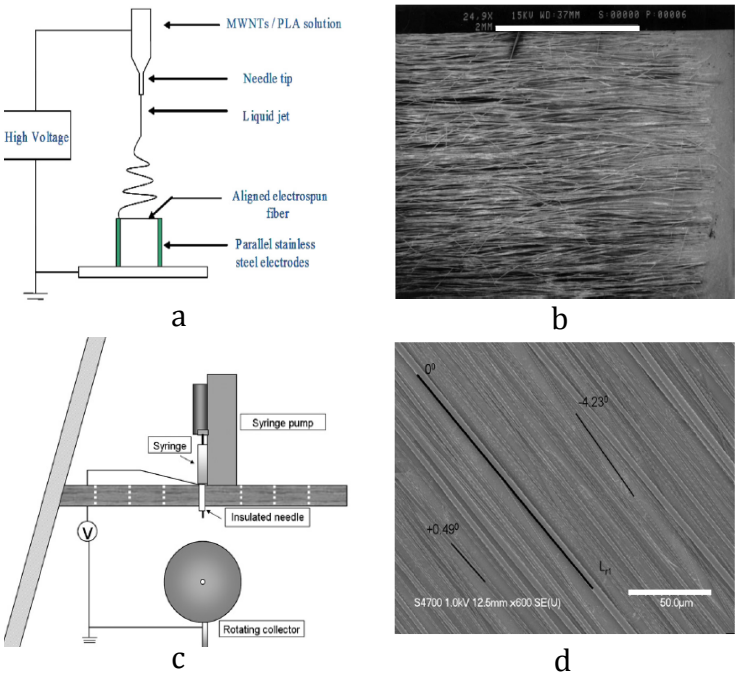

Figure 1.4.a. Schematic of electrospinning setup with parallel stainless steel collector [16], b. illustration of electrospinning setup with a drum collector (scale bar is 2 mm) [18], c and d. SEM images of aligned electrospun fibers (scale bar is 50 µm) [18, 19].

The main disadvantages of co-axial electrospinning involve the demand for specialized equipment and a narrow range of the polymers that can be used in this technique; to overcome the difficulties, emulsion electrospinning has been proposed by a number of groups, including Yang et al. and Xu et al., in which only one nozzle is utilized to produce core-shell fibers [19,20]; in emulsion electrospinning the entity intended for the core is dispersed in a highly volatile

material and vigorously stirred. Afterwards the shell solution is prepared with a water-soluble polymer and the two solutions are mixed and vigorously stirred. Consequently, the electrospun fibers fabricated by this method possess a core-shell structure without the use of co-axial nozzles.

It should be mentioned that melt electrospinning is also a well-known type of electrospinning in which the polymer solution is replaced by a molten polymer. On the one hand, melt-electrospinning holds the advantage of producing fibers with smoother surfaces as opposed to spinning polymer solutions, due to the fact that no solvents are used in the process thus eliminating surface pores caused by the evaporation of the solvent while subject to high voltage. On the other hand, high temperatures are required to melt the polymer in melt electrospinning in addition to the fact that because of the higher viscosity of the molten polymer, the fabricated fibers often possess larger diameters in average compared to those prepared by simple electrospinning. Moreover, lower flow rates of 0.02-0.05 ml/ hr are an inevitable disadvantage of melt electrospinning particularly for the industrial applications of the fibers [5,22].

1.3. Applications of electrospinning

Over the years, electrospun fibers have found their way into the scientific community as well as industry through a variety of applications. These applications vary from the usage of fibers in biomedical engineering to applying fibers in the textile industry. Some of the well-explored applications of

electrospinning are further discussed in this section to emphasize the important role of this method.

1.3.1. Electrospinning in biomedical engineering

The field of biomedical engineering has been using electrospun fibers for diverse objectives; one of the most common applications of electrospinning in biomedical engineering is in drug delivery systems due to the fact that it offers flexibility in the type of material it can carry. The choice of the drug may include DNA, antibiotics or even cancer treatment drugs and the release mechanism of the drug can be controlled to be through a diffusion route or the release of the drug by scaffolding degradation depending on the chosen polymer which can either be biodegradable or non-biodegradable. In addition to embedding the drug of choice in the polymer fibers by means of simple electrospinning, encapsulation of the drug may be done by co-axial electrospinning or emulsion electrospinning [11].

The benefit of using fibers with encapsulated therapeutic agents in drug delivery systems is their capability to perform sustained drug delivery to suppress the burst release of the drug [23], which is crucial for the case of controlled release drug therapy.

Another area of biomedical engineering interested in electrospinning is tissue engineering. Electrospun fibers, especially nanofibers, are used as scaffolds for tissue regeneration of bone, neural, vascular and tendon tissues. Controlling the governing parameters of electrospinning as well as the choice of material can modify the properties of the fibers. Furthermore, the surface of the prepared fibers

may be loaded with bioactive molecules to obtain the desired characteristics for tissue growth or reconstruction [11].

Since the fibers used in tissue engineering are applied in-vivo, a crucial requirement is choosing biocompatible and biodegradable materials; the former requirement is key to avoid the stimulation of the immune system and the latter is essential to ensure the degradation of the fibers after they have served their function and the consequent replacement by the regenerated tissue [24]. Particular tissues in the body, namely in the musculoskeletal system which need to perform functions in a certain direction, such as bearing mechanical load, require uniaxial regeneration. For this purpose, aligned fibers are a perfect candidate to guarantee the reconstruction of the tissue in a specific orientation [11,25]. Electrospinning is also used for purposes of wound healing amongst other application in biomedical engineering [5].

1.3.2. Application of electrospinning in sensors

The vast world of sensors is always welcoming of new methods to increase the sensitivity and selectivity of different kinds of sensors. Electrospinning has proven to be a non-complex effective approach to produce fibers incorporated with a diverse range of materials, which can be used in sensors or even act as sensors themselves. Nanofibers are particularly desirable since the sensing properties are enhanced as dimensions reach sub-micron levels with properties such as high specific surface area and high density of sensitive sites [26].

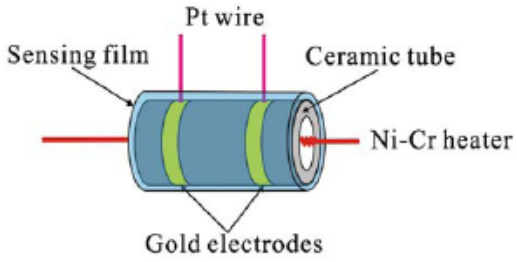

Figure 1.5. Illustration of the toluene sensor designed by Song et al. [28].

Numerous reports have been published on the application of nanofibers in sensing; recently, Du et al. have produced formaldehyde gas sensors with electrospun hetero-nanofiber composites using two jets with opposite polarity [27]. Moreover, Song et al. have manufactured a toluene sensor with reasonable sensitivity, response time and reproducibility based on ZnO-SnO_2 nanofiber webs. The gas sensor was made by creating a paste from the nanofiber web and pasting it on gold electrodes printed on a tube, which was heated by a Ni-Cr wire inserted inside the tube. An illustration of the sensing device in this report is provided in Fig.1.5. The results indicated that the ZnO-SnO_2 composite nanofibers containing a molar ratio of 2:1 throughout all the ratios studied were the most sensitive to 100 ppm of toluene (Fig.1.6).

The plot in Fig.1.6 also implies that the highest level of sensitivity was achieved at an operating temperature of 360 °C which is attributed to the work temperature at which oxygen species on the surface are activated [28].

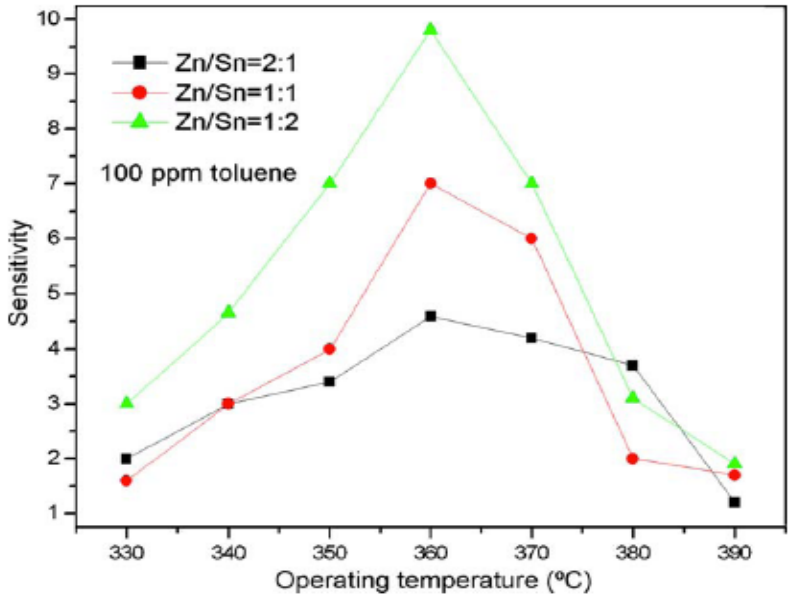

Figure 1.6. The comparison between the sensitivity of the toluene sensors with different molar ratios at different temperatures [28].

These examples only represent a small portion of the application of electrospun fibers in sensors and there are countless accounts of sensing with the assistance of electrospun products [26,29,30,31].

1.3.3. Filtration based on electrospinning

As stated before, the first commercially recognized application for electrospinning was in filtration. A number of the properties of electrospun fibers that make them attractive for filtration applications include high surface area per unit volume,

high porosity, interconnected pore structure which increases permeability, wide range of pore size from nanoscale to microns and high permeability. Electrospun fibers, especially nanofibers, can be used as separation membranes in air purification, water filtration and effluent treatment. Albeit, the disadvantage of using electrospun nanofibers is that they do not possess enough mechanical strength to act as membranes and require additional support. To provide the extra strength, nanofibers are commonly sandwiched between layers, mixed with micron fibers or placed over a support [32].

A well-known usage of nanofibers in this field is in air filters. It has been reported that by coating crude filter material that mainly consist of micron size paper mats with electrospun nanofibers the lifetime of the filtering system is improved by a factor of 10. The mechanism is explained as follows; by the increase in the number of trapped particles up to a certain limit, filters without nanofiber reinforcement can lose their functionality as a result of an increased pressure drop across the filter as well as an additional remaining pressure drop after the filter is cleaned which consequently lead to the need to replace the filter. By adding nanofibers however, the particles are captured at the surface and cleaning the filter will result in a major reduction of the dropped pressure thus increasing the lifetime of the system. In order to improve the efficiency of the filter even more, permanently charged nanofibers can be produced by corona polarization or triboelectric polarization. Triboelectric polarization can be performed on polymers with triboelectric properties [5]. The application of electrospun nanofibers as

water filters is explained in Section 1.4.1.

1.4. Water treatment

Treatment of water is a general term that describes the processes involved to remove harmful contaminants and undesirable substances from water entirely or reduce them to a permitted amount to render the water acceptable for its intended purpose. Water treatment is a vast area and various methods have been established to prepare clean water depending on the unwanted entity in water. Some of the better-known methods of water treatment are discussed in this section.

1.4.1. Separation methods

Separation methods are mainly physical water treatment methods that are commonly used to remove solids from the water. These methods mainly consist of filtration techniques. Conventional separation methods involve distillation, adsorption, and extraction amongst other processes and more recent methods include novel membrane separation, customized polymer absorbents, molecular sieves, etc. [33, 34].

In conventional separation processes, water is flowed through a selection of bed materials such as sand, diatomaceous earth or coarse anthracite coal combined with fine sand that make up pore structures, i.e., filters. Particles in suspension are removed by means of various routes, namely adsorption to the grains of the filter,

coagulation of the particles going through the filter pores (chemical treatment), biological mechanisms or sedimentation [35].

Novel treatment methods such as membrane separations and ultrafiltration take advantage of cost effective operations, high efficiency, compactness and energy efficient procedures [33]. Nanofiltration, which falls into the category of ultrafiltration, has gained immense attention due to benefiting from attributes of nanotechnology as well as its capability to remove particles with finer size, while it may have its disadvantages such as fouling and the generation of concentrate [36]. Even though nanofilters originally served the purpose of softening water by low-pressure reverse osmosis, they were gradually developed to perform combinatory processes to remove a variety of organic and inorganic compounds along removing water hardness [37].

Amongst all the techniques introduced to the field of nanofiltration, the recent efforts to incorporate electrospun nanofibers into water filtration are noteworthy. As mentioned before, nanofibers benefit from porous surface structures, high surface to volume ratio as well as controllable pore size in the nanofiber membrane web. In a recent study by Ma et al., electrospun silica microfibers with a nonporous electrospun SiO_2 nanofiber core and a mesoporous SiO_2 shell were utilized to investigate the sorption of heavy metal ions from wastewater. The microfibers were produced by a combination of electrospinning and sol-gel method and were eventually functionalized with a thiol group to improve the

performance of the fibers. Afterwards the fibers were utilized to examine the sorption of Pb^{2+} and Cd^{2+} ions. Fig.1.7 demonstrates the adsorption of the ions by the fibers with and without the functionalized thiol group called nSiO2@mSiO2 and SH-nSiO2@mSiO2, respectively, vs. time. The plots indicate the successful adsorption of the ions by the fibers that was enhanced by the addition of the thiol group. The enhancement was reportedly caused by the affinity of the heavy metal ions Pb^{2+} and Cd^{2+}, which are soft acids, to the thiol group, which is a soft base. The chemical adsorption is an addition to the physical adsorption by the fibers [38].

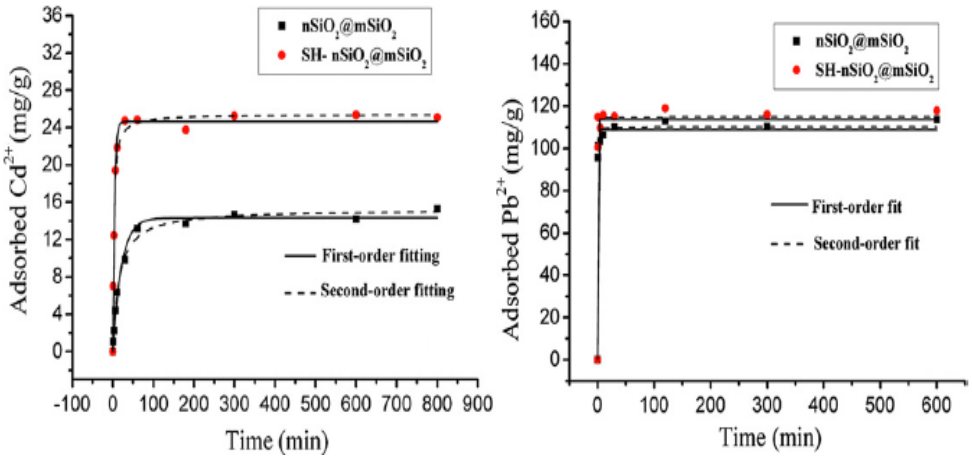

a b

Figure 1.7.a. The adsorption of Cd^{2+} by nSiO2@mSiO2 and SH-nSiO2@mSiO2 vs. time, b. the adsorption of Pb^{2+} by nSiO2@mSiO2 and SH-nSiO2@mSiO2 vs. time [38].

1.4.2. Chemical methods

Chemical water treatment involves the removal and reduction of foulants in water by means of chemical reactions, hence the name. Several methods have so far

been proposed to satisfy the need for the treatment of water using chemical methods such as chemical adsorption, coagulation, disinfection, ion exchange and oxidation treatments amongst others, which will be briefly explained in this section.

1.4.2.1. Chemical adsorption

In water treatments involving chemical adsorption, impurities tend to adsorb on the surface of the adsorbent either do to hydrophobicity of the impurity or in the case of using activated carbon, the affinity of the material to carbon or a combination of both. In general, the tendency to adsorb to another solid for water solutes may arise from electrical charge exchange or van-der-Waals attractions, which are physical processes, or the chemical reactions between the functional groups of the impurity and the absorbent [39]. The advantage of using adsorption methods, which involve chemical as well as physical processes, is the fact that the adsorption filters can be modified to be highly selective. Adsorption membranes are also capable of removing a wide range of contaminants with different sizes; the disadvantage of this method however is being relatively slow.

1.4.2.2. Coagulation

Coagulation, which is normally followed by flocculation, is an important method of water treatment that uses two approaches to remove unwanted particles; the first is to neutralize charges on colloids present in the water so they agglomerate while undergoing flocculation and the second is to provide a bridge between

particles with the same charge by adding other materials (entanglement). Although colloids are like-charged particles in nature, the electrical double layer surrounding each particle prevents the attraction of these charged particles and renders them highly stable. In coagulation by neutralization, charged intermediates are introduced to the aqueous medium which are adsorbed on the colloid particles and reduce the thickness of the double layer as well as the overall charge. In sweep coagulation, amorphous hydroxide precipitates are formed to entangle the particles [40]. While coagulation is a very effective method in the elimination of colloids, its drawback is that a secondary flocculation step is always required.

1.4.2.3. Disinfection

As the presence of pathogenic microorganisms in water particularly drinking water is highly hazardous, the process of disinfecting the water is crucial. These microorganisms include viruses, bacteria and protozoans and their concentration in water should be minimized to negligible, risk free amounts. Although pathogens can be removed physically, most of them undergo disinfection by inactivation. Chlorine and ozone have been traditionally used as disinfectants; however, the process of chlorination is often accompanied by the production of by-products such as chlorophenols, which also possess health threats. An alternative method to disinfection by disinfectant agents is UV irradiation, which is widely used in water treatment [40].

1.4.2.4. Ion exchange

Another method of water treatment is ion exchange in which harmful substances such as mercury, lead and nitrites are removed by means of ion exchangers and ions like Ca^{2+} and Mg^{2+} which are responsible for water hardening are replaced with cations of Na, K and H. The use of Ion exchanger resins in water purification has many advantages; firstly, different layers of resin can be applied to remove different hazardous ions from water. Secondly, since ion exchange is a reversible process, the bed of resins can be revived by the reverse process and returned to the aqueous media. Ion exchange can also be very selective by modifying the chemical structure of the resin. Natural and artificial forms of zeolite, a microoporous mineral made up of aluminosilicates, are also used as ion exchange adsorbents; however, ion exchange resins hold the advantage of having flexible networks with non-uniform width [41].

1.4.2.5. Oxidation treatments

Conventional oxidation methods include the same processes that are used in disinfection, i.e., chlorination, ozonation and photolysis by UV irradiation. However, oxidation conducted by photolysis requires high levels of UV irradiation compared to disinfection of water. To overcome this issue, advanced oxidation processes (AOPs) that benefit from the generation of hydroxyl radicals have been introduced. AOPs include a number of methods; ozone advanced oxidation, which is different from ozonation in the sense that ozonation relies on the direct oxidation of the contaminants in water, oxidation by ozone combined

with UV irradiation, UV/H_2O_2 oxidation, Fenton's reagent and photocatalysis [42]. Photocatalysis is extensively discussed in chapter 2 in Section 2.3.

Oxidation may also be used to assist in other aspects of water treatment, namely in coagulation, increase in the biodegradability of natural organic matter (NOM) and lysis of algal and cyanobacterial cells. The downside of oxidation is that incomplete mineralization of contaminants leads to the production of by-products; these by-products, especially in the case of chlorination, may include harmful materials as discussed in Section 1.4.2.3 [40].

1.5. $BiFeO_3$ (BFO)

Multiferroic materials are a rare group of materials that exhibit at least two orders of ferroic properties as seen in Fig.1.8. This means that in these materials magnetization can be induced by applying an electric field and electric polarization can be induced by applying a magnetic field. Amongst the exclusive group of materials showing this coupling are $TbMnO_3$, $LuFe_2O_4$, $GaFeO_3$ and $BiFeO_3$ (BFO).

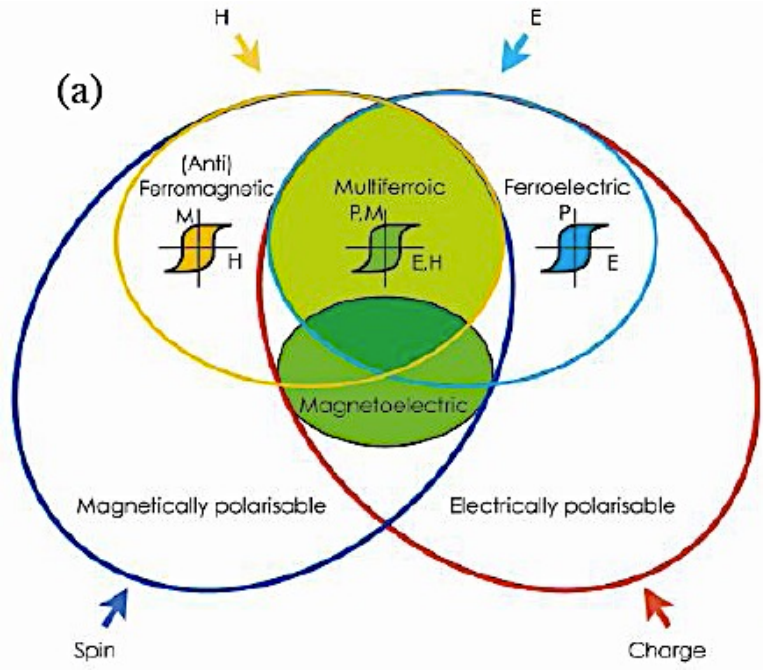

Figure 1.8. Portrayal of multiferroics possessing magnetic and ferroelectric properties [43].

BFO was introduced in the 1960s and its physical properties although controversial have been investigated. The structure of BFO is distorted perovskite with rhombohedral lattice symmetry belonging to the R3C space group [44]; this means that the lattice system does not belong to the cubic system family. A schematic of the perovskite structure of BFO is illustrated in Fig.1.9. The brown spheres demonstrate the position of the A cations in the typical ABX_3 stoichiometry of perovskite structures, which in this case is the Bi^{3+}; the yellow spheres represent B cations (Fe^{3+}) and finally the blue spheres which stand for the position of X atoms, here oxygen.

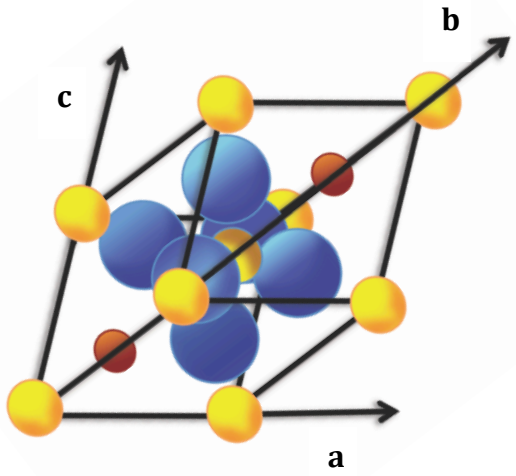

Figure 1.9. Schematic of the R3C rhombohedral perovskite unit cell.

BFO is one of the few materials that exhibits multiferroic properties at room temperature with a Neel temperature of approximately 643 k (380 °C), which indicates the limit to which the antiferromagnetic property of the material exist, and a Curie temperature of about 1123 k (850 °C), which represents the temperature up to which the ferroelectric property of BFO is sustained [44].

BFO is also a semiconductor and its optical properties have been investigated by a number of groups. The focus of this study is the application of the optical band gap and the photocatalytic activity of BFO, which will be discussed in chapter 2.

Chapter 2: Literature review

In chapter 2, an overview on what has already been investigated in the literature concerning the major topics related to the present work is discussed. The electrospinning process and parameters, water treatment based on photocatalysis as well as the motivation behind this research are presented.

2.1. The Electrospinning process

As mentioned in Section 1.2, as the voltage applied to the polymer droplet reaches a certain threshold, the tip of the Taylor cone ejects a polymer solution jet. The process that the jet undergoes afterwards is fascinating. This process was best described by the work of Reneker et al.; their findings provided explanations for the trend in which the polymer jet acts before it eventually reaches the collector.

Firstly, they observed that the jet travels in a straight manner for a short distance prior to splitting into a series of bends. The reason for the formation of a straight segment in the electrospinning process is stated to be the longitudinal stress as a result of the external electric field that stabilizes the jet [9]. An image of the straight segment of the polymeric jet can be seen in Fig.2.1.a.

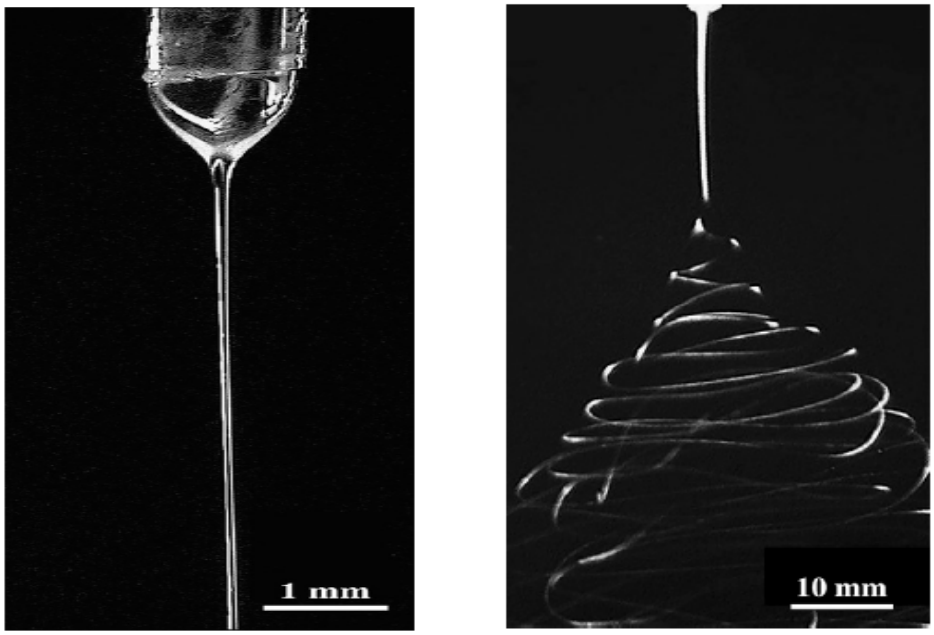

a b

Figure 2.1.a. Straight segment of an electrospinning jet, b. the conical envelope forming from the straight polymer jet [45].

Secondly, the path that the jet takes after it splits was observed and the bending instability dominating the process was expressed by a three-step cycle. In the first step, the straight jet splits into a series of bends, which subsequently begin the second step by forming spiraling loops that continuously grow in diameter as the bends are elongated; this collection of spiraling loops is called a conical envelope (Fig.2.2.b); step 3 commences as the diameter of the conical envelopes increases and the diameter of the cross section of the jet decreases thus fulfilling the conditions for the instability cycle to repeat itself, this time on a smaller level. The cycles continue until the jet meets the target.

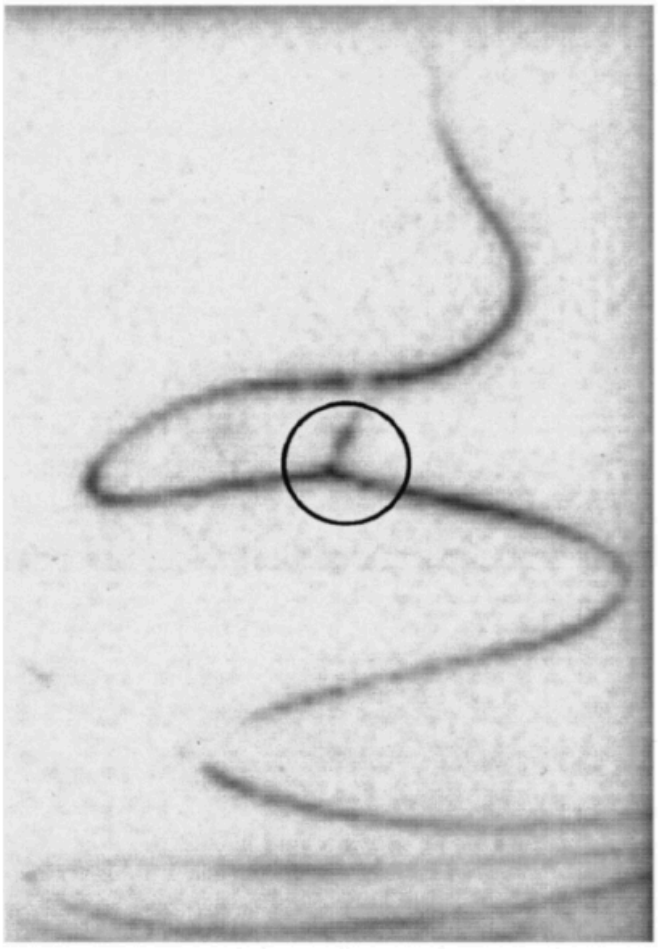

Figure 2.2. Splaying of a branch out of the main electrospinning jet [9].

The commencement of the second step is attributed to the repulsion of the like-charged polymer jet bends that all form the conical envelope. It is worthy to note that at times a branch of the jet “splays” out of the envelope often with a 90 ° angle with the main jet [9]. An example of such splaying is shown in Fig.2.2.

Since many applications of electrospinning rely on the production of fibers with diameters falling in the nanometer range as well as a narrow size distribution, it is

beneficiary to study the phenomena surrounding the formation of fibers that determine the final diameter and distribution. The two chief phenomena in this matter are the thinning of the fibers as the jet is elongated in the conical envelope and the number of cycles the jet undergoes before hitting the collector.

2.2. Electrospinning parameters

Similar to all scientific experiments, electrospinning is governed by two categories of parameters, i.e., material parameters and process parameters. Both categories play a significant role in controlling the hydrodynamic and electrostatic processes that occur in electrospinning. In this section, some of these variables are examined.

2.2.1. Material parameters

A variety of polymer materials are used in the electrospinning of fibers. The characteristics of the polymer as well as the solvent used in the preparation of the polymer solution (excluding melt-spinning) could significantly affect the electrospinning process. The most influential parameters in this category are those attributed to the polymer material used, namely the choice of polymer and its molecular weight (MW), the solvent with regards to the solvent type and vapor pressure and finally the parameters of the prepared solution which include the concentration of the polymer solution, viscosity, surface tension, electrical conductivity and rheological properties. The most important of these parameters are further explored here.

Tiwari et al. investigated the effect of the concentration of the solution and the consequent viscosity of the polymer solution on electrospinning by examining different concentrations of PLGA, poly (lactide-co-glycolide), an 80:20 ratio copolymer of PLA (poly (lactic acid)) and PGA (poly (glycolic acid), with a molecular weight of 152 kDa electrospun under fixed process parameters. The results of this study indicated that the viscosity of the solutions increased with solution concentration and the log-log relationship between the two parameters could be expressed with two lines as seen in Fig.2.3.

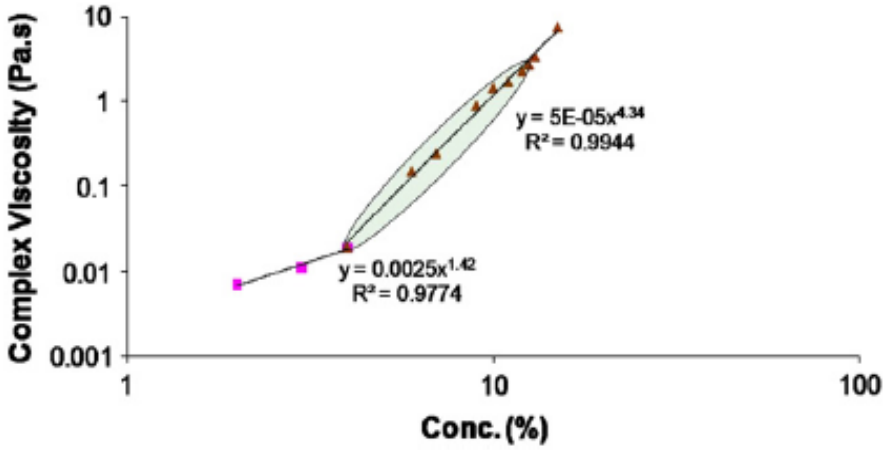

Figure 2.3. The relationship between the viscosity of prepared PGLA solutions with concentration in a log-log base [46].

Furthermore, the influence of the increase in concentration from on the electrospun products was studied by electrospinning PLGA solutions (PLGA in a 80:20 mixture of chloroform and DMF) of different w/v ratios. SEM images of the fibers formed from the electrospinning of different concentrations were also presented (Fig.2.4).

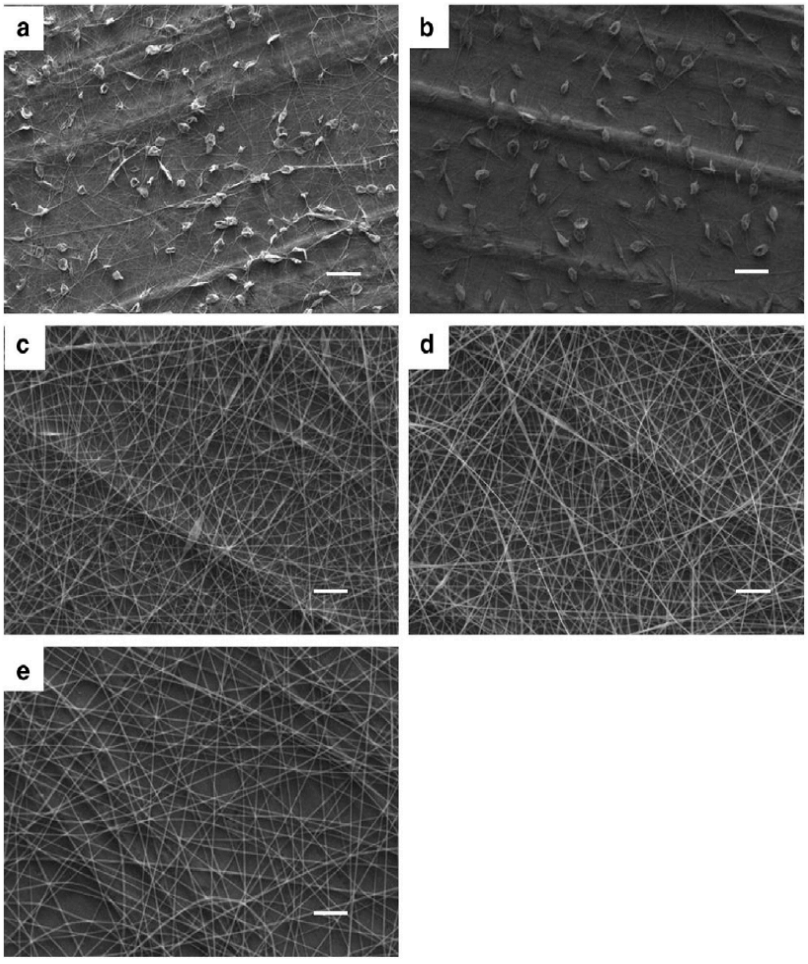

Figure 2.4. SEM images of electrospun fibers for concentrations of a. 2%, b. 3%, c.4%, d.5% and e.8% w/v of PLGA with the scale bars in all images representing 10 μm [46].

It was observed that for solution concentrations of 2% and 3% the fibers contained so called beads which diminish the continuous cylindrical morphology of the fibers (Fig.2.4.a and Fig.2.4.b) and the beads were transformed from a spherical shape to a spindle type, respectively; at concentrations of 4% and higher however, overall beadless fibers were witnessed with an exception of a negligible number of beads in concentration of 4%. Electrospinning of concentrations of less than 2% led to no fiber formation and the use of a concentration of approximately 12% deemed the electrospinning process difficult as the solvent would evaporate at the tip of the nozzle before the process was completed [46].

The role of the vapor pressure of the solvent can be found among the results of a thorough study on the effective parameters on electrospinning carried out by Theron et al.; PEO (poly (ethylene oxide)) solutions were prepared using water as the solvent as well as a mixture of water and ethanol while maintaining the overall concentration of the polymer solutions. All solutions were electrospun and it was concluded that the solidification of nanofibers was assisted by the increase in ethanol content even though the volume charge density was lowered as a result of the decreasing number of charge carriers by the replacement of fractions of water with ethanol [47]. What this implies is that by choosing a solvent with a higher vapor pressure, while the solution undergoes an electric field during electrospinning the solvent evaporates more quickly leading to the formation of nanofibers before the electrospinning jet reaches the collector. The other effect of the evaporation of the solvent is on the morphology of the fibers and the faster the

solvent evaporates, the more porous electrospun fibers become on the surface [48]. An SEM image of porous PLLA (poly (l-lactic acid)) fibers with dichloromethane can be seen in Fig.2.5.

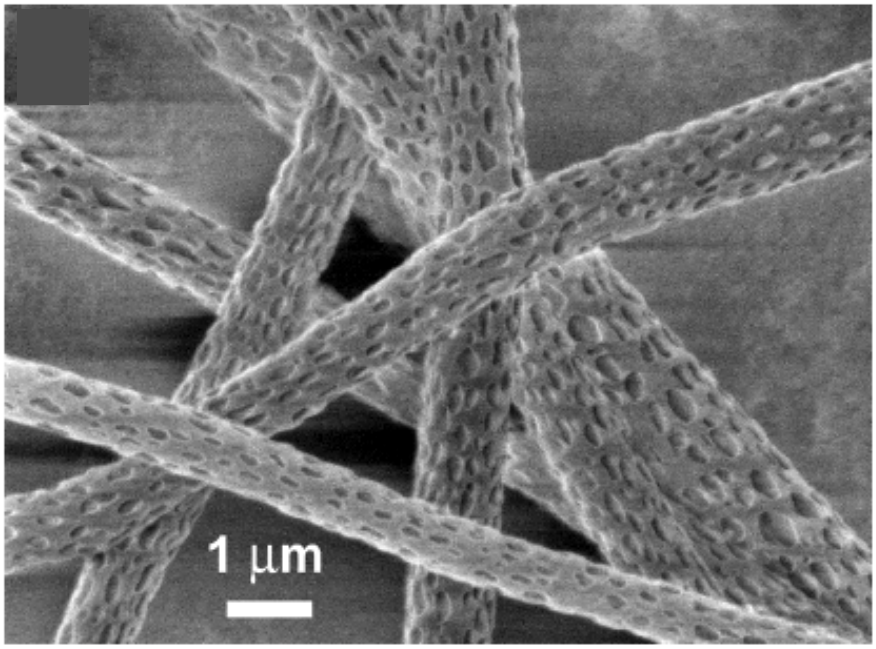

Figure 2.5. SEM image of porous electrospun PLLA fibers [48].

Molecular weight of the electrospinning polymer affects electrospinning in such a way that by the increase of the molecular weight of the polymer, the diameter of the electrospun fibers increases and as far as the morphology of the fibers goes, since any factor influencing the viscosity of the solution affects the morphology of electrospun fibers, beadless homogeneous fibers are formed at higher MWs and as MW decreases, the concentration of beads increases; this was reported by Ojha et al. [49].

2.2.2. Process parameters

Through the 13 parameters influencing the results of an electrospinning process, applied electric field (voltage by distance ratio), distance between the nozzle and the collector, feeding rate of the solution (flow rate), ambient conditions such as temperature and humidity and nozzle orifice diameter are listed as the effective process parameters [50].

Since the process of electrospinning is mainly reliant on the application of high voltage, it is crucial to mention the effect of the applied voltage on the final electrospinning products. As mentioned before, the applied voltage should be high enough for the electrostatic forces to overcome the surface tension of the droplet formed at the tip of the nozzle in order for the polymer jet to successfully form from the Taylor cone. The effect of further increasing the applied voltage has been investigated by many groups [47,51,52,53,54,55].

While Li et al. and Pornsopone et al. reported that by increasing the applied voltage the diameter of the electrospun fibers increases [52,55], Gu et al. stated that the applied voltage had insignificant impact on the fiber diameter and standard deviation of the diameter [53] which is in agreement with what Yördem et al. suggested for solutions with higher concentration, especially at higher collector distances [51]. On the other hand, Lee et al. presented data indicating that there was an optimum voltage at which the fine fibers were achieved; the study demonstrated that as the voltage increased up to 20 kV, due to the increase

of the electrostatic forces, the splitability of the jet was enhanced and the higher net charge density guaranteed the lower surface tension of the jet which all resulted in the formation of finer fibers. Nevertheless, as the applied voltage was further increased to 25 kV a loop structure was developed as a result of severely reduced surface tension.

The effect of the distance between the nozzle and the collector has also been studied over the years throughout many electrospinning related studies [50,51,54,56]. Yördem et al. observed that increasing the distance resulted in the formation of finer fibers, especially in the nano-scale [51], which was similar to the results reported by Lee et al. [54]. Although the effect of the combination of voltage-distance i.e., the applied electric field has not been investigated as extensively as the effect of these two parameters individually, Sukigara et al. reported that by the increase in the electric field the diameter of the electrospun fibers decreases [57].

As mentioned, the flow rate of the electrospinning material also affects the process. One the one hand, if the flow rate is too low the formation of a continuous jet from the Taylor cone becomes improbable since there is not enough polymer solution to support the Taylor cone as the voltage is applied. On the other hand, if the feeding rate of the polymer solution is too high the chance of droplets dripping on the electrospun jet increases [58]. Thompson et al. reported that finer diameter of electrospun fibers is achieved at lower flow rates and

increasing this parameter tends to increase the fiber diameter as well as the diameter of beads [50]. That said, the influence of altering the flow rate between the two extremes on the diameter of fibers is suggested to be negligible according to a number of reported studies although fiber morphology is affected by it [59-61].

All in all, as stated by Heikkilä et al. there always exists a contradiction between the reported results involving different parameters influencing fiber diameter and size distribution [58] and to obtain desirable fibers there is a need to optimize the electrospinning process by means of finding an optimum combination of different parameters.

2.3. Water treatment based on photocatalysis

Photocatalysis, utilized as a well-known advanced oxidation process for water treatment, holds the advantage of direct absorption of light as its main energy source at room temperature where there is no thermal activation necessary to fully mineralize pollutants [62,63]. Photocatalysis involves photolysis, the breaking down of a chemical compound by the assistance of photons, which is accelerated by means of a catalyst.

Photocatalysis can occur in the form of homogeneous as well as heterogeneous photocatalysis; in the former, photocatalysts such as ozone are used and the reactants exist at the same phase as the catalyst. In the latter however, the reactants are in a different phase from the catalyst that triggers various oxidation

and reduction reactions through which the contaminating agent is degraded [63]. Direct photolysis by UVC also leads to a series of homogeneous reactions in the solution when the photodecomposition of excited organic compounds leads to the breaking down of the molecules into smaller molecules [64]. Semiconductors are often applied in the heterogeneous type of photocatalysis. In this case, photocatalysis is activated when photons with sufficient energy excite the electrons of the valence band in the photocatalyst, causing the electrons to jump to the conduction band thus leaving behind holes and creating electron-hole pairs. Due to the presence of contaminants (especially organic donors), the recombination of the electrons and holes is delayed, the holes react with the moisture on the surface of the photocatalyst and a series of oxidative reactions with so called hole scavengers such as the contaminants are triggered; the electrons in turn participate in a chain of reductive reactions with the oxidants in the environment. Ergo, the pollutant is degraded into harmless final products such as CO_2 [63].

In aqueous solutions where oxygen is present, conduction band electrons can be scavenged by oxygen and form superoxide ions ($O_2^{\bullet -}$) and protonated hydroperoxyl radicals ($H_2O^{\bullet}$) as seen in Eq.2.1 and Eq.2.2, respectively.

$$O_2 + e^- \rightarrow O_2^{\bullet -} \qquad (2.1)$$

$$O_2^{\bullet -} + H^+ \rightarrow H_2O^{\bullet} \qquad (2.2)$$

$H_2O^{\bullet}$ can in turn form H_2O_2 by combining with electrons and holes:

$$H_2O^{\bullet} + e^- \rightarrow H_2O^- \quad (2.3)$$

$$H_2O^- + h^+ \rightarrow H_2O_2 \quad (2.4)$$

Holes may also react with the water molecules and generate hydroxyl radicals:

$$H_2O + h^+ \rightarrow OH^{\bullet} + H^+ \quad (2.5)$$

These interactions assist in the prevention of electron-hole recombination and organic donors can scavenge the generated holes before recombination occurs [65]. The direct photodegradation of the contaminating agent occurs by the reaction between the harmful entity and the photogenerated holes which leads to the production of intermediate or final degraded compounds (Eq.2.6). $OH^{\bullet}$ radicals assist photocatalysis by indirect photodegradation of hazardous compounds (Eq.2.7).

$$R + h^+ \rightarrow R^{+\bullet} \rightarrow \text{Intermediate/Final Degradation Products} \quad (2.6)$$

$$R - H + OH^+ \rightarrow R'^{\bullet} + H_2O \quad (2.7)$$

Moreover, a series of mass transfer and reaction steps make up the entire photocatalysis process and when mass transfer steps are much faster than the reaction steps, mass transfer steps do not limit the general reaction rate of photocatalysis and reaction steps determine the rate [66].

The most explored semiconductor in photocatalysis is indubitably titanium oxide (TiO_2), also known as titania. Titania is a well-suited candidate for photocatalysis due to its beneficial characteristics of stability in water, inexpensiveness and high photocatalytic efficiency as a result of its high quantum yield [67].

Different structures of TiO_2 have been investigated in the field of photocatalysis; reports have been published on TiO_2 nanoparticles [68-70], nanofibers [67,71,75], nanotubes [72], thin films [73,74] and even flower structures [70] to name a few.

Hussain et al. reported the synthesis of TiO_2 nanoparticles (TNP) by means of sol-gel process and the photocatalytic activity of TNP was investigated and compared with TiO_2 prepared by solution combustion method (TSC) and commercially available Degussa P25. The prepared nanoparticle samples proved to have the highest surface areas amongst all the samples and the range of the optical band gaps of the samples ranged for 3.00 eV to 3.26 eV with the TNP prepared by sol-gel exhibiting a band gap of 3.17 eV. The photodegradation of Ethylene with different TiO_2 samples is illustrated in Fig.2.6.

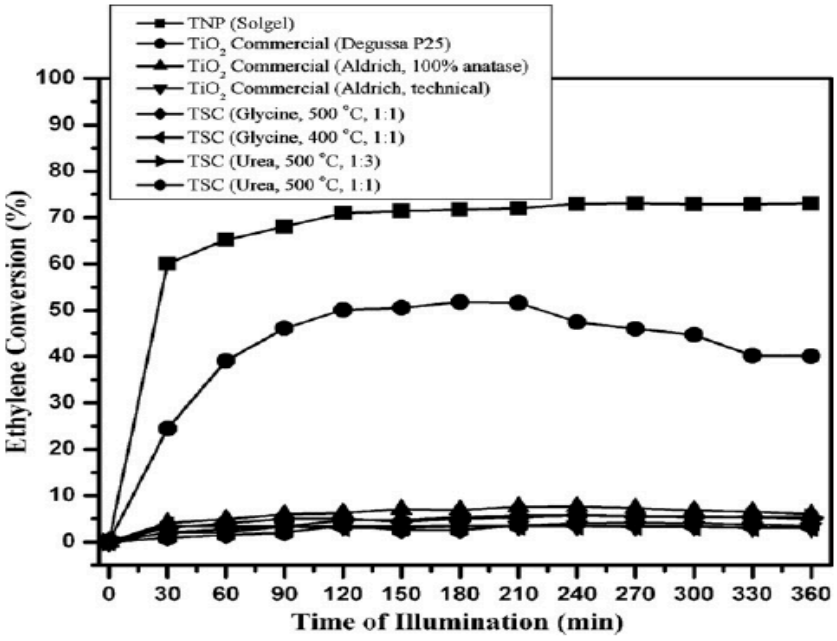

Figure 2.6. The photodegradation of Ethylene with time using different TiO2 samples [69].

Their results indicate the dramatic increase in the photodegradation of Ethylene when the TNP are applied [69].

In a study by H. Choi et al. anti-biofouling, photocatalytic, separation and disinfection properties of nanostructured crystalline TiO_2 thin films and TiO_2/Al_2O_3 composite membranes was investigated in the decomposition of creatinine and methylene blue, the destruction of biological toxins (microcystin-LR) and the inactivation of pathogenic microorganism (Escherichia coli). Fig.2.7.a and Fig.2.7.b demonstrate the photocatalytic activity of the TiO_2 thin films on the destruction of microcystin-LR (MC-LR) and the inactivation of Escherichia coli (E. coli), respectively.

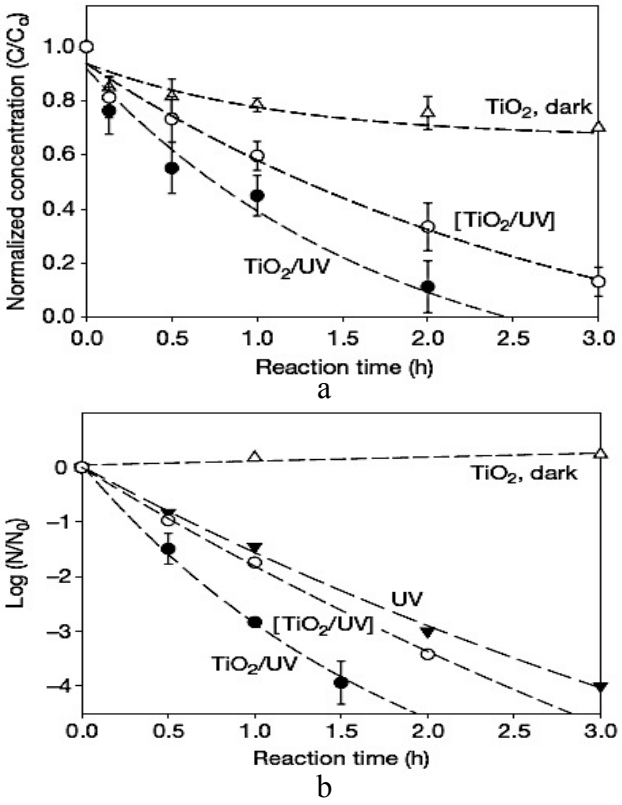

Figure 2.7.a. The destruction of MC-LR and b. the inactivation of E-coli vs. reaction time by the photocatalytic activity of TiO_2 thin films.

The comparison between the results obtained by TiO_2 thin films combined with UV irradiation and the control systems indicates the successful photodegradation and inactivation of the harmful entities. Moreover, the anti-biofouling properties of the TiO_2/Al_2O_3 composite thin films were confirmed by the results from the treatment of waste water containing different concentrations of dissolved solids (DS) and dissolved organic carbon (DOC) as seen in Fig.2.8.a; Fig.2.8.b also shows the photodegradation of methylene blue and creatinine by applying TiO_2 thin films [74].

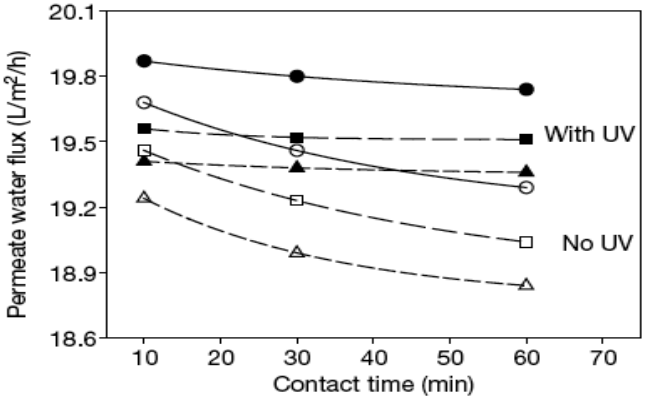

a

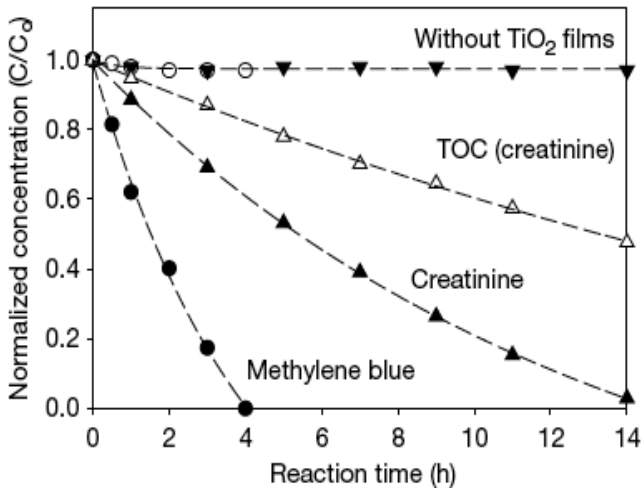

b

Figure 2.8.a. The anti-biofouling activity of TiO_2/Al_2O_3 thin films on circle: DS_{200}-DOC_{30}, square: DS_{400}-DOC_{60}, and triangle: DS_{800}–DOC_{120}, b. photodegradation of methylene blue and creatinine [74].

In 2010, S. Choi et al. stated the superiority of electrospun TiO_2 nanofibers in terms of hydrogen generation as a result of photocatalytic activity [75]. One apparent advantage of nanofibers over structures such as nanoparticles is the fact that nanofibers can be used as membranes and therefore no further measures need to be taken for the removal of the photocatalysts from the water, especially when treating drinking water. Laera et al. demonstrated that TiO_2 nanofibers were comparable with the commercial TiO_2 Degussa P25 in the degradation of Congo Red (CR) and Carbamazepine (CBZ) in saline water and municipal effluent furthermore concluded that the nanofibers are easily separable from the aqueous medium. They also stated that the although the use of lamps to intensify the process in large applications of solar photocatalysts is neither cheap nor environmentally friendly compared to solar based processes, it holds the advantage of using less energy and chemicals in addition to mild reaction conditions over other advanced oxidation processes [71].

A study on the concurrent filtration and solar disinfection and photodegradation of Ag/TiO_2 nanofiber membranes by Liu et al. showed that the application of these membranes in water purification was promising. The investigation was initiated by preparing TiO_2 nanofibers by means of electrospinning and subsequent calcination and Ag/TiO_2 nanofibers were synthesized by coating the TiO_2 nanofibers with Ag nanoparticles; Ag/TiO_2 membranes were prepared along with commercial P25 and pure TiO_2 membranes for comparison. The photocatalytic disinfection experiments were carried on E. coli and degradation experiments

were conducted on methylene blue as a model contaminant. An SEM image of the Ag/TiO_2 nanofibers can be seen in Fig.2.9.

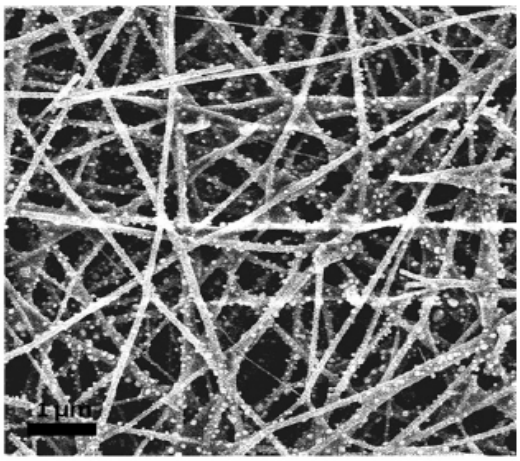

Figure 2.9. SEM image of Ag/TiO_2 nanofibers; the scale bar of the image is 1μm [67].

Fig.2.10 demonstrates the surviving fraction of E. coli in different systems. The data acquired indicates that the Ag/TiO_2 nanofiber membranes combined with UV irradiation were the best system applied and an additional $OH^{\bullet}$ scavenger test confirmed the enhancement of bacteria inactivation by photocatalytic activity of the nanofiber membranes.

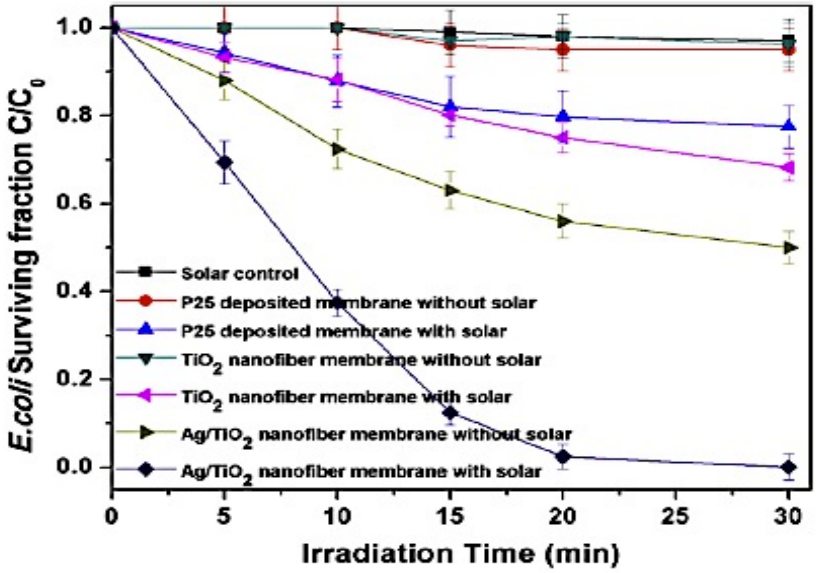

Figure 2.10. The disinfection of E. coli by applying different systems [67].

A comparison between the degradation of methylene blue vs. irradiation by direct photolysis, P25 membrane, TiO_2 membrane and Ag/TiO_2 membrane is illustrated in Fig.2.11.a and applying Ag/TiO_2 shows to be the most effective system; the reusability of the Ag/TiO_2 with UV irradiation by washing between degradation cycles is indicated in Fig.2.11.b in terms of the total organic carbon vs. irradiation time [67].

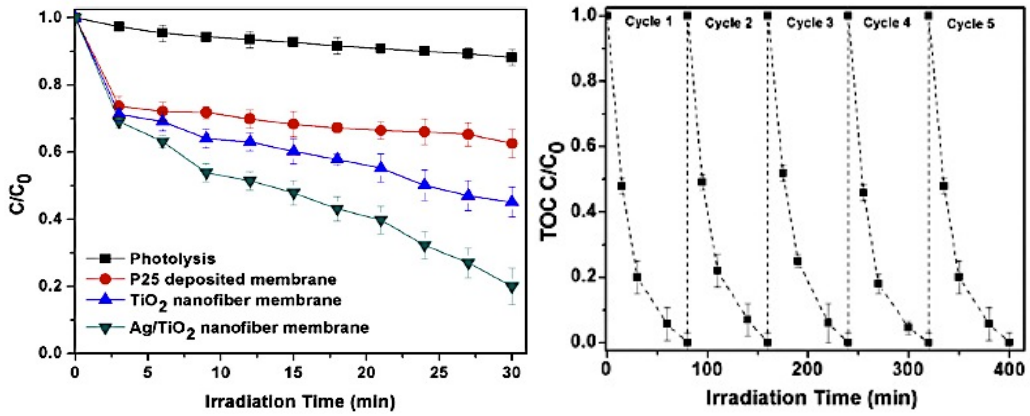

a b

Figure 2.11.a. The degradation of methylene blue vs. irradiation time in different systems, b. reusability of Ag/TiO_2 nanofiber membranes in the degradation of methylene blue [67].

2.4. Motivation

The introduction of $BiFeO_3$ (BFO) as one of the few materials exhibiting multiferroic properties at room temperature augmented the interest in this semiconductor; the discovery of the photocatalytic activity of BFO brought light to new opportunities for the application of BFO in water purification. As band gap values are size dependent, the band gap energy of BFO has been reported to be in the range of 2.5-2.8 eV by Ihlefeld et al. [76] as well as Hauser et al. [77]; however, value of 2.2 eV has also been stated in the literature for nanostructured BFO particles [78]. What lies common in the aforementioned reports is the indication that BFO has a smaller band gap compared to the band gap energy of 3.2 eV for TiO_2 (band gap value of TiO_2 extracted from report by Chong et al. [66]). Xu et al. reported the degradation of CR by applying BFO thin film under visible light irradiation, which proved to be economic as well as reproducible.

Their results indicated an approximate 16 % decrease in the contaminant concentration in roughly 240 min [79]. In a similar study, Gao et al. utilized BFO in the forms of bulk and nanoparticles in order to degrade methyl orange under the two regimes of irradiation namely visible and UV-Vis irradiations. The results presented the decrease in the concentration of the methyl orange under both irradiation regimes and also for both structures; however, the most significant degradation occurred when BFO nanoparticles were utilized under UV-Vis exposure. In other words, decreasing the size of the BFO from bulk to nanoparticles increased the efficiency. Moreover, using a more energetic irradiation with a wavelength in UV-Vis range instead of visible light enhanced the photodegradation of the methyl orange (Fig.2.12)[80].

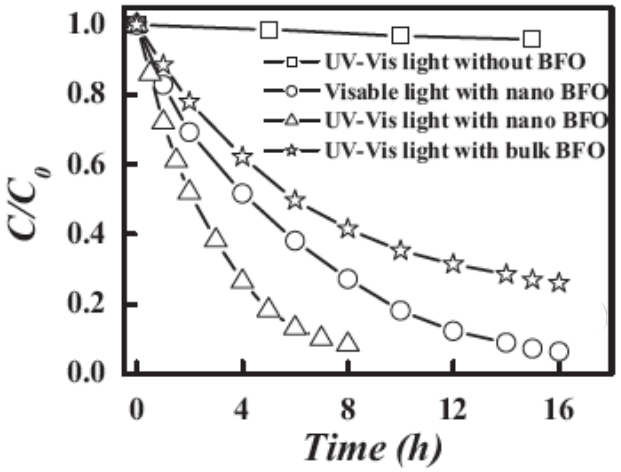

Figure 2.12. The different rates of the degradation of methyl orange using UV-Vis light without BFO, visible light with nanoparticles of BFO and UV-Vis light with bulk BFO and BFO nanoparticles [80].

Notwithstanding the reports, to the best of the knowledge of the author no study has yet been done on the photocatalytic activity of one-dimensional BFO nanostructures in water purification. Given the fact that BFO is a relatively new material and one-dimensional BFO nanostructures have only recently been developed, exploring their benefits in the field of water treatment holds great merit. The mechanism of the photocatalytic activity of BFO nanofibers is illustrated in the schematic in Fig.2.13.

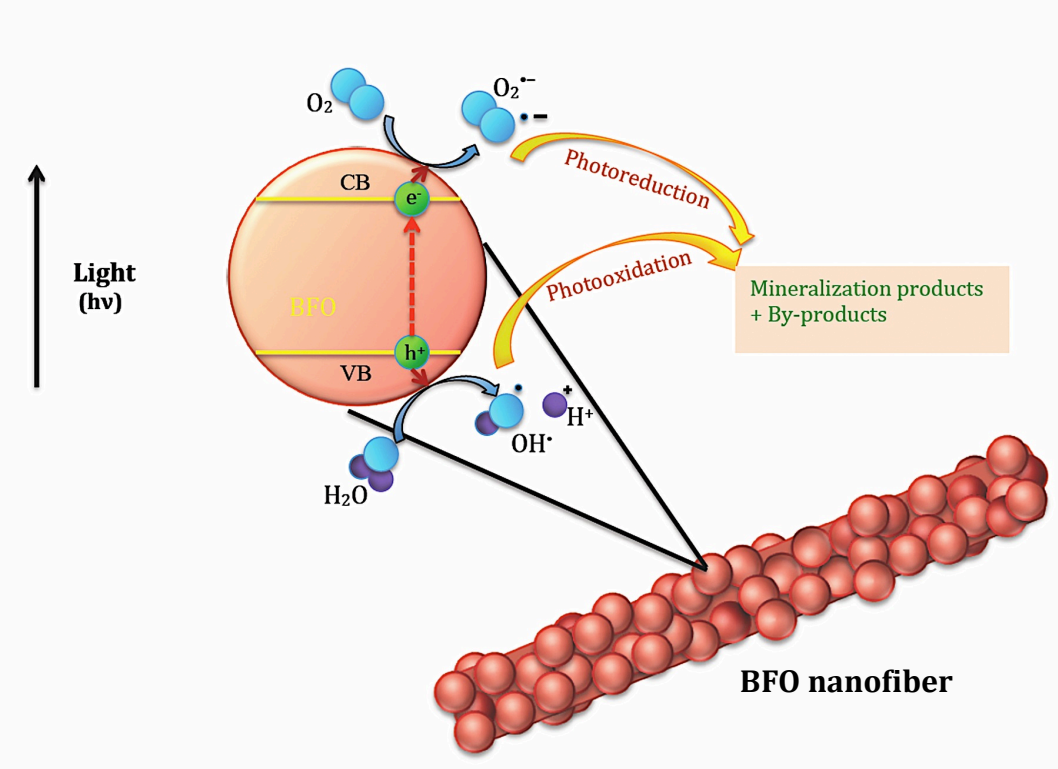

Figure 2.13. The schematic of the photocatalytic mechanism of the BFO nanofibers.

In this study, a homemade electrospinning setup is constructed and optimization measures are taken to find conditions in which the finest fibers with narrowest size distribution can be achieved. BFO/Nylon6 fibers are fabricated and BFO nanofibers are obtained by calcination at 600 °C. The detailed electrospinning

process and subsequent measures to prepare the nanofibers are reported as well as characterization techniques. 4-Chlorophenol (4CP), a harmful organic compound which is found in pesticidal chemical industries, petrochemical industries and a common chemical intermediate in effluent chlorination [81] is chosen as a model contaminant to investigate the degradation capability of photocatalytic electrospun BFO nanofibers. The degradation behavior of 4CP in aqueous solution in the presence of BFO nanofibers under UV irradiation is investigated. Furthermore to study the role of the nanofibers in 4CP degradation, changes in the aqueous solution containing the contaminant subject to UV irradiation in the absence of BFO nanofibers is examined. The governing kinetics of the photocatalytic process is also explored based on a pseudo-first order kinetic model.

Chapter 3: Experimental

In this chapter, the materials and methods utilized throughout the process of this research are discussed. The methods section consists of different fabrication and characterization processes as well as the photodegradation studies.

3.1. Materials

Nylon6 in the form of pellets with a molecular weight of 11202 g/mol and Formic acid with a purity greater than 98 % where purchased from Sigma Aldrich (Canada) to prepare the polymeric solution. For the purpose of synthesizing the Bismuth Ferrite, Bismuth (III) nitrate pentahydrate with a purity of 98 % (Acros, USA), 99.99 % pure Iron (III) nitrate nonahydrate (Sigma Aldrich, Ontario, Canada) were obtained alongside 2-Methaxyethanole (Acros, USA), Ethanolamine with a purity more than 99.5 % purified by resdistillation (Sigma Aldrich, Ontario, Canada) and Glacial Acetic acid with a purity of 99.7 % (Fisher Scientific, Canada).

High purity 4-Chlorophenol (≥99 %) with a molecular weight of 128.56 was acquired from Sigma Aldrich (Canada) to be utilized as water contaminant.

3.2. Methods

3.2.1. Homemade electrospinning Setup Assembly

A homemade horizontal electrospinning device was assembled in the laboratory in accordance with conventional electrospinning apparatus requirements (Fig.3.1).

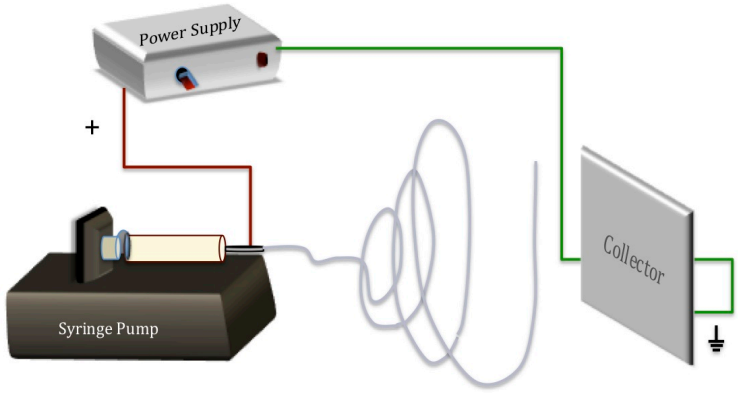

Figure 3.1. Schematic of the homemade electrospinning apparatus consisting of 3 main components: High voltage power supply, syringe pump and collector.

As seen in the schematic figure of the electrospinning setup (Fig.3.1), the homemade apparatus consists of 3 main parts; these parts are a high voltage power supply, a syringe pump and a grounded collector, which are discussed in detail in the following sections.

3.2.1.1. Dc-Dc high voltage module

In electrospinning systems commercially available, high voltage is commonly supplied by means of an Ac to Dc power supply which acts as the most crucial part of the electrospinning apparatus; however, in order to increase the mobility of

Table 3.1. Specifications of the high voltage module.

Input Voltage	12 V, Dc
Output Voltage	0-25 kV, Dc
Power	4 W
Current	0.19 mA

the entire system as well as to lower manufacturing costs, the high voltage power supply was chosen to be a 25A series Dc to Dc high voltage module (Ultravolt, USA), with the specifications indicated in Table 3.1. An image of the module as received is illustrated in Fig.3.2.a.

An Ac to Dc adaptor was used to supply permanent input voltage of 12 V to the module. The module was then positioned in a stainless steel box to insure further grounding and to ease operation while enabling manual adjustments in the output voltage as shown in Fig.3.2.b. The output voltage cord was connected to the nozzle and the ground wire was set to be clipped to the collector.

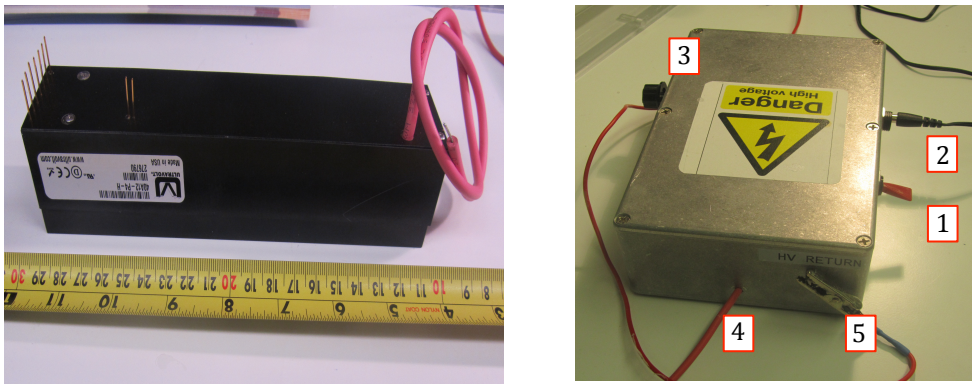

a b

Figure 3.2.a. Dc-Dc high voltage power supply as received b. Stainless steel box containing the high voltage module with 1. On/Off switch, 2. 12 V Dc Input, 3.Voltage adjustment knob, 4. High voltage output cord, 5. Grounding cord.

In order to maintain a safe environment for the electrospinning setup working with high voltage, a polyacrylic shield was designed to contain the electrospinning jet (Fig.3.3).

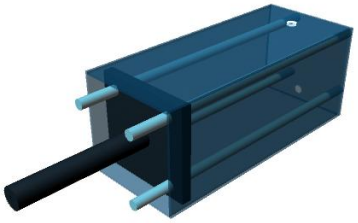

Figure 3.3. Poly acrylic high voltage shield for the electrospinning setup.

3.2.1.2. Syringe pump

The syringe pump in an electrospinning device is used to ensure a continuous flow of the polymer solution as well as to retain the flow at a fixed rate

throughout the electrospinning process. For these purposes, a Fisher Scientific single syringe pump (Fisher Scientific, Canada) capable of providing flow rates between zero and 426 ml/hr and dispensing volumes from 10 µl to 60 ml was utilized in the electrospinning device.

3.2.1.3. Grounded collector

The collector or target in an electrospinning setup is the platform on which the electrospun products are formed and this collector may be in different geometries and sizes to control the final product. For this homemade setup a 20 cm × 20 cm aluminum sheet was chosen to be the primary collector.

3.2.2. Electrospinning setup optimization[1]

In order to investigate the effect of electric field systematically, a series of experiments consisting of 64 test conditions were carried out with changes in the voltage in the range of 7.5-25 kV and the distance between the two electrodes in the range of 7.5-25 cm. All the experiments were performed at ambient temperature. Nylon6 solution with the concentration of 15 wt% was used as a model polymer. The solution was prepared by dissolving a sufficient amount of the Nylon6 pellets into formic acid and stirring magnetically until a homogenous transparent solution was obtained. The solution was transferred into a 5 ml plastic syringe with a gauge 21 needle (OD of 1.270 mm and ID of 0.838 mm). The solution flow rate was kept constant at 0.3 ml/hr. The diameter and the size distribution of the fibers were investigated using a scanning electron microscopy

(SEM, VEGA-3, Tescan, USA) with the accelerating voltage of 20 kV. All samples were sputter coated with gold prior to the SEM analysis. To determine the average diameter and the size distribution of the fibers, 100 fibers were chosen randomly from each sample SEM image.

3.2.3. BFO nanofiber fabrication and characterization

3.2.3.1. BFO solution preparation by sol-gel method

Bismuth (III) nitrate pentahydrate and Iron (III) nitrate nonahydrate salts with a 1.05:1 w/w ratio were dissolved in 2-Methaxyethanol and stirred until a homogeneous solution was obtained. Subsequently, to set the pH of the solution to 4, a sufficient amount of Ethanoamine was added. Furthermore, Glacial Acetic acid was used to control the viscosity of the BFO solution to suit the feasible viscosity range of the sequent electrospinning. The entire BFO sol-gel precursor solution was then magnetically stirred for 2 hrs at room temperature. 15 wt% Nylon6 solution was prepared by dissolving Nylon6 pallets in Formic acid and followed by magnetic stirring; the final BFO/Nylon6 solution to be electrospun was made by adding the BFO solution drop by drop to the Nylon6 polymer solution with a 1:1 v/v ratio while being magnetically stirred to obtain a homogeneous solution.

[1] The procedure presented in this section has been published in the Journal of Scanning Microscopies, DOI 10.1002/sca.21044.

3.2.3.2. BFO/Nylon6 electrospinning and calcination

The voltage of the electrospinning apparatus for electrospinning the prepared BFO/Nylon6 solution, carried in a 5 ml plastic syringe, was set to 20 kV applied through a 21-gauge stainless steel needle. The separation distance between the metallic nozzle and the aluminum collector, which was grounded, was set to be 20cm. The flow rate of the solution was fixed at 0.3 ml/hr and the electrospinning experiments were conducted at ambient temperature. For the purpose of easily characterizing the electrospun products, $Pt/Ti/SiO_2/Si$ substrates were also attached to the collector. The electrospun material was then dried in a vacuum oven (282A, Fisher scientific, Canada) at 125 °C for 1 hr and further calcinated at 600 °C for a duration of 2 hrs in a furnace (muffle furnace, Fisher Scientific, Canada) in air ambient to eliminate the Nylon6 surrounding the expected BFO nanofibers.

3.2.3.3. BFO nanofiber characterization

Calcinated samples on $Pt/Ti/SiO_2/Si$ substrates were characterized using X-ray diffraction (XRD) (Rigaku, Japan, Cu K_α radiation λ = 1.5405 Å) to determine the phase structure; scanning electron microscopy (SEM) with an accelerating voltage of 30 kV was used to examine the morphology of the as-spun samples as well as calcinated samples; the diameter of the fibers prior to and post calcination was also studied. All samples for SEM analysis were sputtered with gold using a Denton Gold Sputter unit (USA). Field Emission Scanning Electron Microscopy

(FE-SEM, JAMP- 9500F, JEOL, USA) was utilized to determine the crystallite size on the nanofibers; the accelerating voltage of the microscope was set to 15 kV. In order to determine the optical band gap of the BFO nanofibers was investigated by means of UV-Vis spectroscopy (Varian Carey 50, Agilent, USA).

3.2.3.4 Characterization of 4CP

The absorption peak of the contaminant 4CP was found by means of UV-Vis spectroscopy. In order to determine the calibration curve of the contaminant, a plot correlating optical absorbance with concentration, sufficient amounts of 4CP were dissolved in MilliQ water to prepare solutions with concentrations of 1, 2, 5, 7.5 and 10 μg/ml; the absorbance of each solution was examined by UV-Vis spectroscopy.

3.2.4. Water treatment

3.2.4.1. UV photocatalytic degradation of 4CP

The application of the photocatalytic properties of BFO nanofibers in water purification was studied through the photodegradation of 4CP. BFO nanofiber mats on 1.5 cm × 3 cm aluminum substrates weighing 0.5-0.7 mg were suspended in aqueous solutions with various 4CP concentrations of 1, 2, 5 and 7.5 μg/ml, which were prepared by dissolving the 4CP in Milli-Q water. These samples were named 4CP-1, 4CP-2, 4CP-3 and 4CP-4, respectively. The samples were subsequently irradiated by UV light at a wavelength of 385 nm and an intensity of

15 W/cm^2 using a UV lamp (BlueWave LED Prime UVA, Dymax, USA).

2 reference samples of 5 μg/ml were also prepared with no added BFO nanofiber mat; one was irradiated with UV light to determine the effectiveness of the nanofibers in the photodegradation of 4CP (4CP-blank) and the other was left in the dark to see the role of UV irradiation on its own (4CP-dark). In order to guarantee the mass transfer of the contaminant to the surface of the nanofibers, all the water purification studies were conducted as the aqueous solutions were being magnetically stirred. At predetermined time intervals, 1 ml samples were taken from the aqueous solutions for further analysis using UV-Vis spectroscopy; the concentration of the contaminant at designated times was obtained by converting the absorbance values from the calibration curve of 4CP.

All the experiments involving UV irradiation were conducted while samples were being cooled by ice since the high power irradiation source was held close to the samples. The entire degradation setup was placed inside an aluminum-covered box to avoid dangers of UV light exposure. A schematic of the degradation setup is illustrated in Fig.3.4.

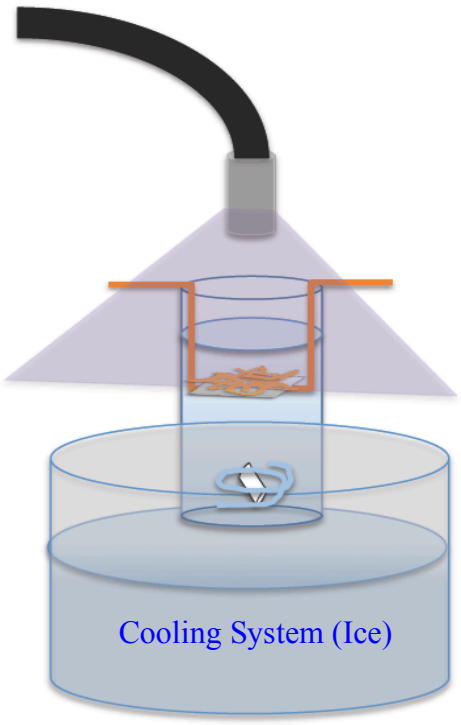

Figure 3.4. Schematic of the setup for the UV photocatalytic degradation of 4CP.

3.2.4.2. Visible light photocatalytic degradation of 4CP

Since Gao et al. demonstrated the photocatalytic activity of BFO nanoparticles under visible range irradiation [80], a series of tests were conducted under irradiation by means of a 100 W light bulb. Samples 4CP-1, 4CP-2, 4CP-3 and 4CP-4 with the same specifications mentioned in Section 3.2.4.1 were subjected to irradiation and 1 ml aqueous solution samples were taken at predetermined time intervals for UV-Vis analysis. A reference solution with an initial 4CP concentration of 5 µg/ml with no BFO fiber mat (4CP-blank) was also subjected to visible light irradiation to investigate the sole influence of the nanofibers; in

addition to that, 4CP-dark was used to see the sole effect of the light bulb. All samples undergoing the experiments were magnetically stirred. The purpose of this series of tests was to determine the potential for the use of visible light photodegradation of the model contaminant when applying BFO nanofibers.

3.2.4.3. Kinetics of degradation

The kinetics of the photodegradation of 4CP based on the photocatalytic activity of BFO nanofibers under UV irradiation was studied using a pseudo-first order model presented in Eq.3.1.

$$ln\left(\frac{C}{C_0}\right) = kt \qquad (3.1)\ [79,82]$$

The C_0 and C values in Eq.3.1 represent the initial concentration of the contaminant and the concentration of the contaminant at a given time, respectively; t is time and k is the photodegradation reaction rate constant [79].

3.2.5.BFO nanogrids

BFO nanogrids were fabricated by a fiber alignment method. The aluminum sheet collector for conventional electrospinning was replaced by an aluminum sheet on a drum collector with a diameter of 3/4 inch (1.905 cm) (Fig.3.5.a) connected to a NF113LG-011 Dc motor with a nominal speed of 22000 rpm (Testco, USA) (Fig.3.5.b) and powered by an E3630A triple output Dc power supply (Agilent, USA). To ground the aluminum target, a grounded wire was brushed against the aluminum.

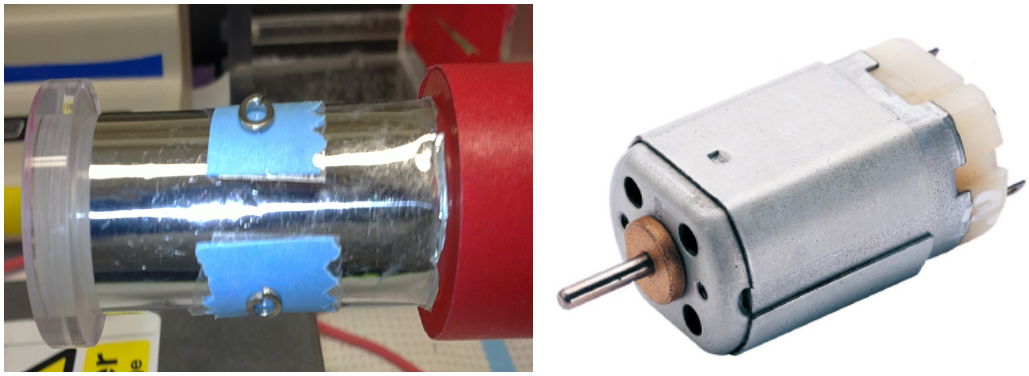

a b

Figure 3.5.a. Drum collector used for the fabrication of BFO nanogrids, b. DC motor used for spinning the drum (courtesy of Testco, USA).

In order to obtain aligned fibers, a series of experiments were carried out by changing the applied voltage, the separation distance between the drum and the nozzle, the rotation speed of the drum (rpm) and time. The next step was to obtain nanogrids by rotating the target 90 ° after the electrospinning of each layer of aligned fibers. The experiments were performed on prepared Nylon6 solutions and once the fabrication of Nylon6 nanogrids was accomplished, BFO/Nylon6 nanogrids were fabricated by this method using the BFO/Nylon6 solution prepared as described in Section 3.2.3.1; further calcination with conditions stated in Section 3.2.3.2 was conducted. Experiments were carried out at ambient temperature and a solution flow rate of 0.3 ml/hr.

Examination of the formation of the nanogrids was done by taking SEM images of the electrospinning products prior to and after calcination. In addition, the average size of the grid pores of the as-spun nanogrids, nanogrids post drying and

after calcination was analyzed using SEM image analysis. The purpose of fabricating the nanogrids was to investigate the potential application of the BFO nanogrids in particulate filtration to be combined with the photocatalytic water treatment in the future.

Chapter 4: Results and discussion

In chapter 4, the results of the experiments of the previous chapter are elaborated and the potential reasons for obtaining these results are discussed. Moreover, the possibility of using the fabricated nanogrids in the future is examined at the end as well as the potential for the usage of visible light in the photodegradation of contaminants.

4.1. Electrospinning setup optimization[1]

In these experiments the electric field was varied in a range of 0 - 3.33 kV/cm by adjusting the applied voltage and the separation distance. The effect of electric field and distance-voltage combinations on the fiber diameters and size distributions were investigated by analyzing the SEM images of the electrospun polymers. We have used three different regimes of electric field. After electrospinning, the collector with electrospun polymer was removed for SEM analysis.

I) $E \leq 0.5$ kV/cm

The SEM images of collector material for electric field in this range showed no signs of fiber formation. This observation might be due to the fact that the electric field were not sufficient to overcome the surface tension of the polymer droplet formed at the tip of the needle; therefore, a charged fluid jet could not be ejected towards the target [83].

[1] The procedure presented in this section has been published in the Journal of Scanning Microscopies, DOI 10.1002/sca.21044.

II) 0.5<E<1 kV/cm

Fig.4.1 illustrates the SEM images of the collector for two different voltage-distance ratios with the electric field lying in the above range. It could clearly be observed that the fibers were formed on the collector; however, the homogeneity of the fiber mat was compromised by the formation of belt-like entities, which are distinguishable from well-known cylindrical fibers. The same line of reasoning that was used for the previous category could be applied in this range of electric field. At the present situation, although the electrostatic forces were high enough to produce fibers they were not sufficient to complete the transformation of the entire polymer solution, thus the formation of belt-like entities was inevitable.

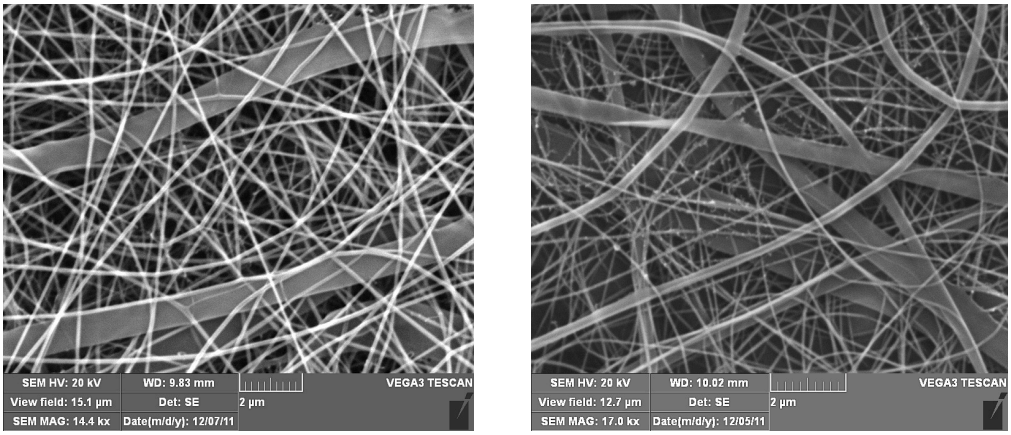

a b

Figure 4.1. The formation of belt-like entities in electrospun products with an applied electric field of a. 0.857 kV/cm, b. 0.6 kV/cm.

III) 1≤E≤3.33 kV/cm

As opposed to the conditions in I and II, a complete formation of the fibers could be realized in this range of electric field as illustrated in Fig.4.2. Even though this electric field range shows the best results in terms of the fiber formation, it

requires further investigation to discern the effect of the electric field on the diameter and the size distribution of the fibers more precisely. This can be achieved by dividing the entire range of this electric field regime into six subgroups of E=1, 1<E≤1.5, 1.5<E≤2, 2<E≤2.5, 2.5<E≤3 and 3<E≤3.33 kV/cm.

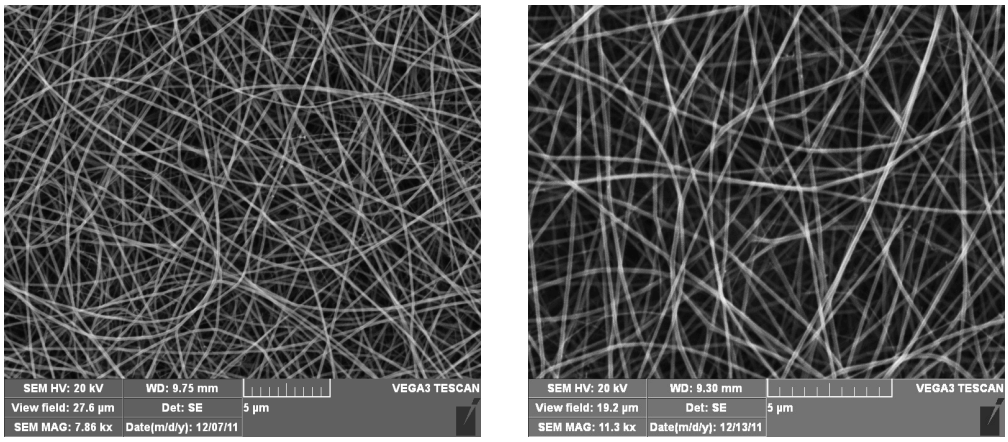

a b

Figure 4.2. Complete formation of electrospun fibers with cylindrical morphology with applied electric fields of a. 1 kV/cm, b. 1.67 kV/cm; scale bars represent 5 µm.

The effect of electric field could be studied from two points of view, namely the average fiber diameter and size distribution. Comparison between average fiber diameters calculated from the SEM images is shown in Fig.4.3. The size distribution of the fibers in each subgroup could be determined by means of standard deviation calculation. Table 4.1 summarizes the results of the standard deviation for each category. As the data in Fig.4.3 suggests, the finest fiber diameter could be achieved by maintaining the electric field at 1 kV/cm as well as 3<E≤3.33 kV/cm; however, the standard deviation data in Table 4.1 indicates that the narrowest size distribution of fibers could be obtained at E=1 kV/cm. Based

on the observations of Reneker et al. on the different steps of a bending instability cycle [9], it could be hypothesized that the two important parameters which determine the diameter and the size distribution of the fibers are the fiber thinning due to the electrostatic forces and the number of bending instability cycles that the jet undergoes.

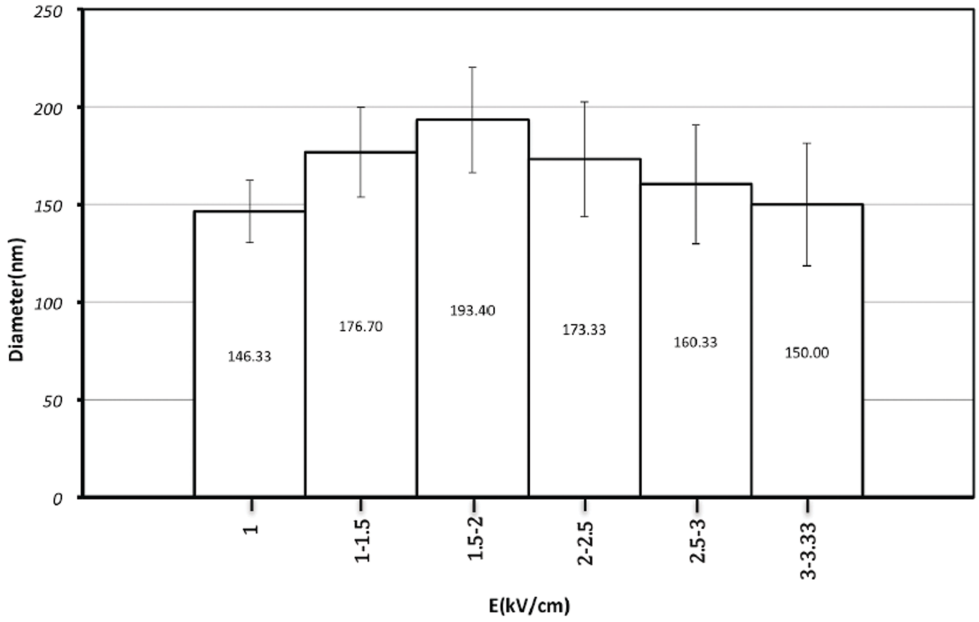

Figure 4.3. The effect of six different electric field ranges lying in the span of $1 \leq E \leq 3.33$kV/cm on the average diameter of the nanofibers. The increase in the electric field caused an initial increase in the average diameter due to the dominant effect of the number of bending instability cycles which followed by a decrease due to dominant effect of fiber thinning at higher electric field.

The trend observed in Fig.4.3 suggests that both parameters could affect the diameter and the size distribution of the fibers; however, it could be inferred that the average diameter is mostly controlled by the electrostatic forces and the size distribution is influenced mainly by the number of bending instability cycles.

Table 4.1. Standard deviation of average diameter of nanofibers with respect to the electric field.

E (kV/cm)	Standard Deviation (nm)
1	16.00
1-1.5	23.00
1.5-2	27.60
2-2.5	30.00
2.5-3	29.82
3-3.5	31.00

The entire trend could be explained based on this hypothesis that increasing the electric field causes the increase in the fiber thinning due to higher electrostatic forces; however, the number of bending instability cycles that the jet could undergo decreases. It has been established by Reneker et al. that bending instability will discontinue if the fiber solidification occurs [9]. Increasing the electric field results in the higher electrostatic forces which consequently causes the solvent to evaporate more quickly and the jet to solidify in less time. The initial increase in the fiber diameter is possibly due to the fact that the number of bending instability cycles is decreasing; however, the effect of fiber thinning is so small that it is unable to compensate the lower number of the cycles. Afterwards, the fiber diameter decreases possibly as a consequence of the high fiber thinning ($2<E\leq3.3$ kV/cm) which could compensate for the low number of bending instability cycles. The ascent in the standard deviation in Table 4.1 could be explained according to the above-mentioned hypothesis. Increasing the electric

field eventually results in the lower number of bending instability cycles and consequently the decrease in the diameter uniformity.

Since E=1 kV/cm could be reached with different combinations of voltage and distance, further investigation was performed on the diameter and the size distribution of fibers amongst all the combinations leading to this electric field. The average diameter and also the size distribution of fibers in each of these combinations are compared in Fig.4.4 and Table 4.2, respectively.

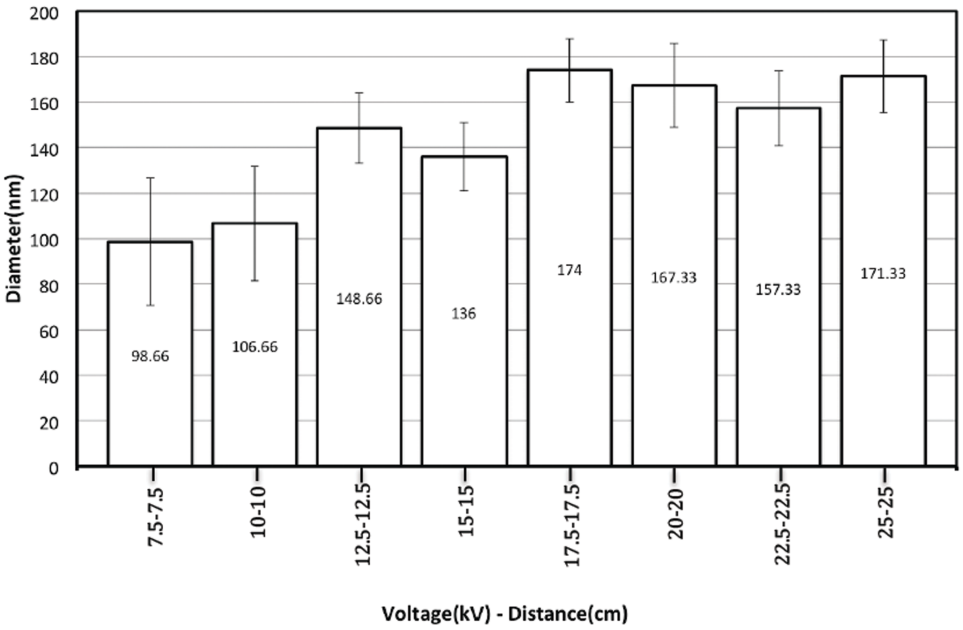

Figure 4.4. The effect of different combinations of voltage and distance with the E=1 kV/cm on the average diameter of the nanofibers.

Considering the results in Fig.4.4, although it could be concluded that the finest fibers could be achieved in the lowest voltage-distance combinations, i.e., 7.5 kV-7.5 cm and 10 kV-10 cm, the standard deviation results, which were summarized in Table 4.2, suggest that these two combinations produce the widest size distributions amongst all combinations. Considering the fiber diameter and size

distribution criteria, it could be inferred that the best combination in order to achieve fine fibers along with a narrow distribution is 15 kV-15 cm. Therefore, in order to prove this hypothesis, the size distributions of 7.5 kV-7.5 cm and 15 kV-15 cm combinations were studied by measuring the size of 100 fibers for each combination in SEM images. The size distribution of fibers at 7.5 kV-7.5 cm and 15 kV-15 cm are illustrated in Fig.4.5.a and Fig.4.5.b, respectively.

Table 4.2. Comparison between the standard deviation of different voltage-distance combinations.

Combination	**Standard Deviation (nm)**
7.5 kV-7.5 cm	27.99
10 kV-10 cm	25.26
12.5 kV-12.5 cm	15.52
15 kV-15 cm	15.02
17.5 kV-17.5 cm	14.04
20 kV-20 cm	15.8
22.5 kV-22.5 cm	16.67
25 kV-25 cm	15.97

It could be observed from Fig.4.5.a that the combination of 7.5 kV-7.5 cm produces many different fiber diameters covering a range from 50nm to 230 nm. However, Fig.4.5.b shows that the combination of 15 kV-15 cm generates a narrower size distribution comprising a range from 90 nm to 180 nm. The same

reasoning as above could be used in explaining the results. Increasing the distance between the two electrodes while maintain the constant electric field will possibly increase the numbers of the bending instability cycles since it allows increased time of flight for the jet. Thus, the combination of 15 kV-15 cm produces narrower size distribution.

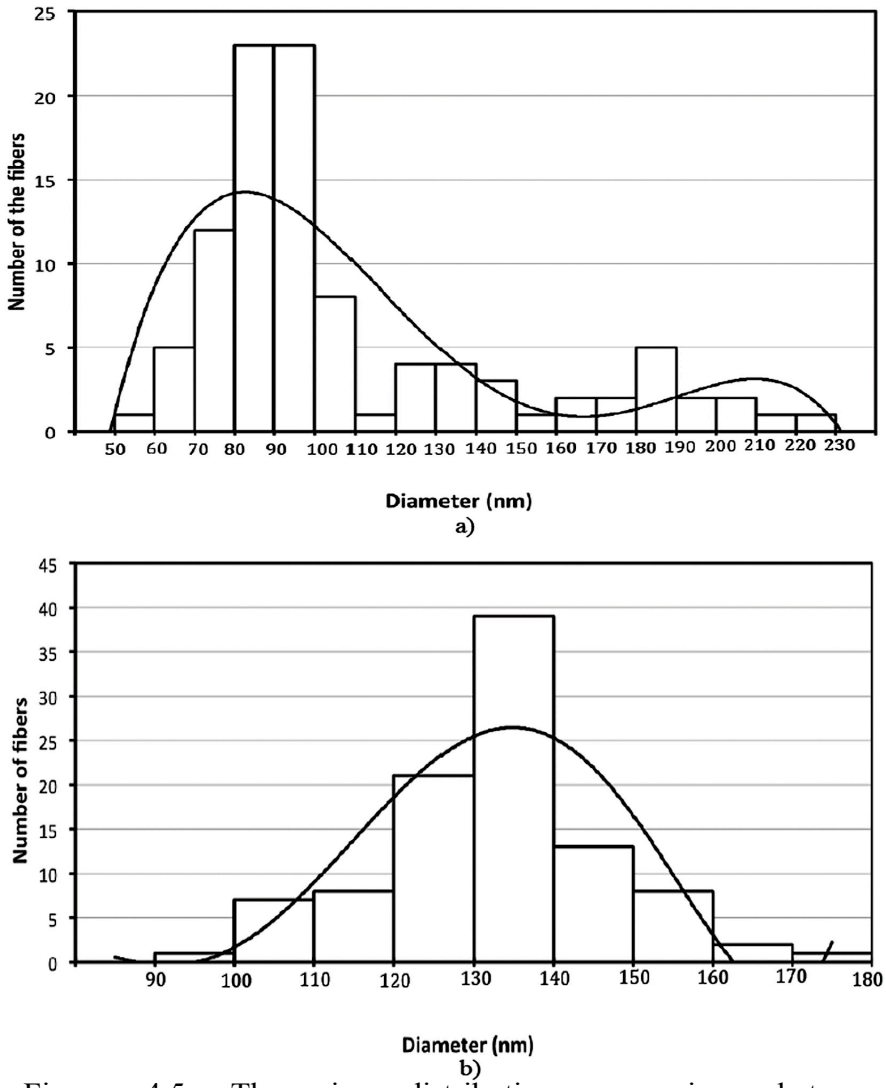

Figure 4.5. The size distribution comparison between combinations a. 7.5 kV-7.5 cm and, b. 15 kV-15cm. Maintaining E=1 kV/cm with the combination of 15 kV-15 cm resulted in a more uniform size distribution of the fibers possibly due to the increased number of bending instability cycles as a result of increased distance.

4.2. Characterization of BFO nanofibers

4.2.1. SEM analysis

Fig.4.6.a shows the SEM image of the as-spun Nylon6/BFO fibers prior to calcination. The formation of continuous cylindrical nanofibers is evident and the average diameter of the as-spun fibers was calculated to be 230 ± 30 nm. The inset of Fig4.6 shows the SEM image of the BFO/Nylon6 nanofibers prior to calcination with a higher magnification. The continuousness of the BFO fibers was not compromised after calcination at 600 °C as seen from SEM image in Fig.4.7.a; with Nylon6 no longer surrounding the BFO nanofibers, the average diameter was decreased to 130 ± 35 nm.

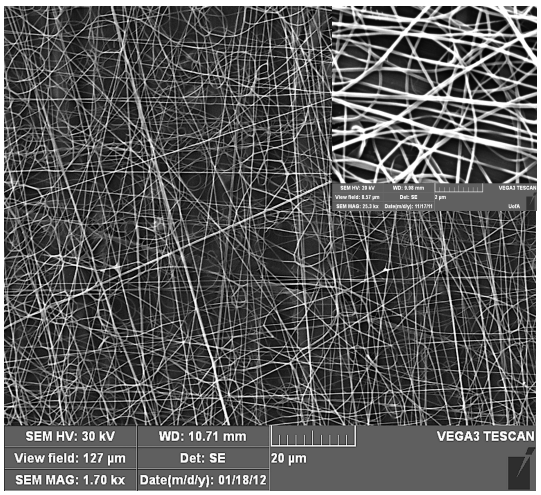

Figure 4.6. SEM image of as-spun nanofibers of BFO/Nylon6 prior to calcination. The image indicates the formation of continuous cylindrical nanofibers; the scale bar represents 20 µm. The inset illustrates the as-spun BFO/Nylon6 nanofibers at higher magnification; the scale bar in the inset measures 2 µm.

The inset of Fig.4.7.a demonstrates the calcinated BFO nanofibers at a higher magnification. The FE-SEM image in Fig.4.7.b shows the BFO crystallites forming continuous nanofibers; the average diameter of the crystallites is observed to be 29 ± 2 nm.

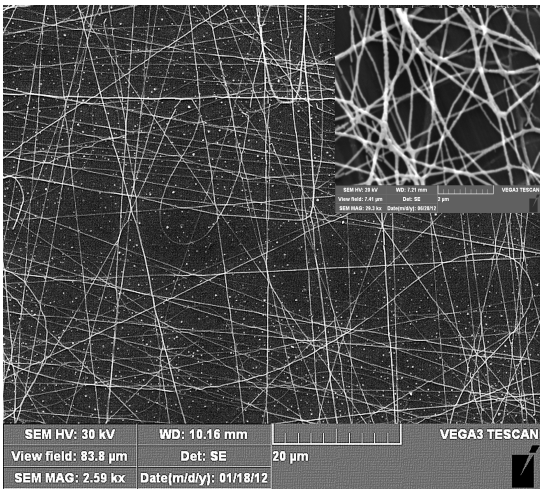

a

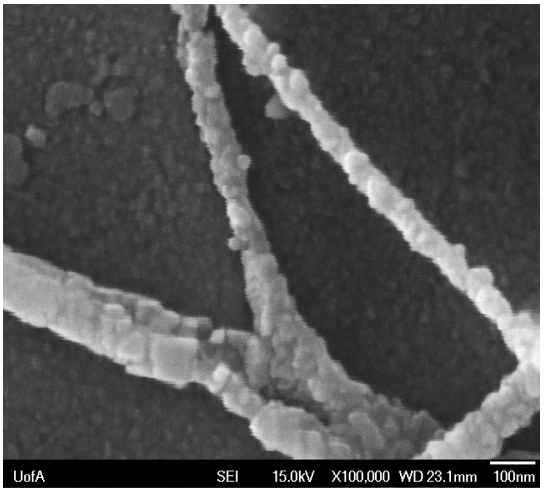

b

Figure 4.7.a. SEM image of the BFO nanofibers after calcination at 600 °C. The integrity of the nanofibers is intact after the elimination of Nylon6; the scale bar represents 20 µm. The inset shows the BFO nanofibers at a higher magnification with the scale bar displaying 2 µm, b. FE-SEM image of the BFO nanofibers after calcination at 600 °C. BFO nanofibers contain BFO crystallite with the mean diameter of 29 ± 2 nm; the scale bar shows 100 nm.

4.2.2. XRD results

Although the SEM images confirmed the formation of BFO nanofibers and the high temperature calcination guarantees the evaporation of the Nylon6 polymer and the crystallization of BFO, to confirm the phase purity of calcinated BFO nanofibers, XRD analysis was carried out. The XRD pattern demonstrated the key characteristic peaks of R3C rhombohedral perovskite BFO matching the reported standard values (JCPDS: 01-071-2494). Peaks matched with Platinum are resultant of the Platinum coated substrate and small traces of the secondary phase $Bi_2Fe_4O_9$ can be distinguished. However, the dominant phase remains to be BFO (Fig.4.8).

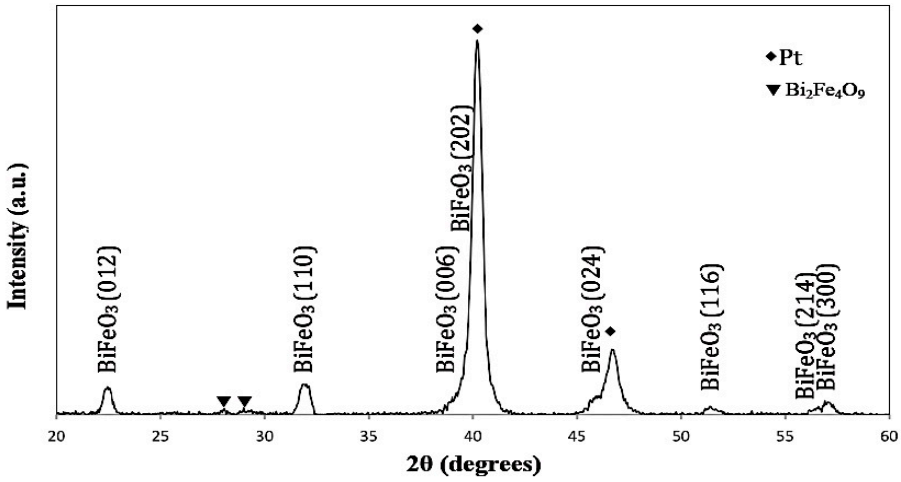

Figure 4.8. XRD pattern of the calcinated nanofibers showing the dominant presence of BFO; Platinum peaks are due to the Pt coated substrate and very small traces of $Bi_2Fe_4O_9$ are found.

4.2.3. Optical band gap of BFO nanofibers

To determine the band gap of the nanofibers, UV-Vis spectroscopy was utilized. The absorbance values from the UV-Vis spectroscopy helps determine the band gap by calculating the absorption coefficient α. The absorbance has a linear

correlation with α as stated in Eq.4.1 where A is the absorbance and l is the cell path length, which for this study was 1 cm.

$$A = \alpha l \qquad (4.1)$$

Absorption coefficient α and energy band gap E_g follow the correlation in Eq.4.2, where β is the number indicative of the nature of the electron transition from the valance to the conduction band; h is Planck's constant and k is a constant.

$$\alpha = (\frac{k}{h\nu})(h\nu - E_g)^{\beta} \qquad (4.2)[84]$$

For a material exhibiting a direct band gap, β is ½ and Eq.4.2 can be written as Eq. (2) in which C is a constant.

$$(h\nu\alpha)^2 = C(h\nu - E_g) \qquad (4.3)[84]$$

Ergo, the direct band gap of the BFO nanofibers is obtained by the intercept of the linear portion of $(h\nu\alpha)^2$ vs. $(h\nu)$. As depicted in Fig.4.9, the intercept suggests that the direct band gap of the BFO nanofibers is approximately 2.5 ± 0.05 eV, which is consistent with reported values by other groups [76,77]. The inset in Fig.4.9 illustrates the absorption data acquired for the nanofibers by UV-Vis spectroscopy from which α is determined at each wavelength.

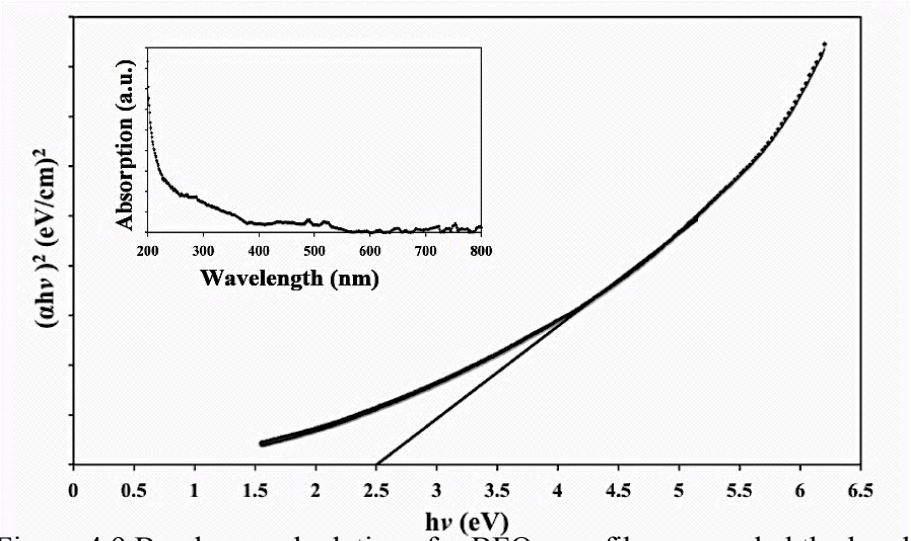

Figure 4.9 Band gap calculations for BFO nanofibers revealed the band gap energy of 2.5 ± 0.05 eV. The inset shows the absorbance of the nanofibers for the irradiation by the light in range of 200-800 nm.

4.3. Characterization of 4CP

The absorption peak of 4CP was obtained by means of UV-Vis spectroscopy (Fig.4.10). The spectrum indicates an absorption peak at a wavelength of 225 nm, which was used in finding the calibration curve of the contaminant as well as the absorbance data in the water treatment experiments.

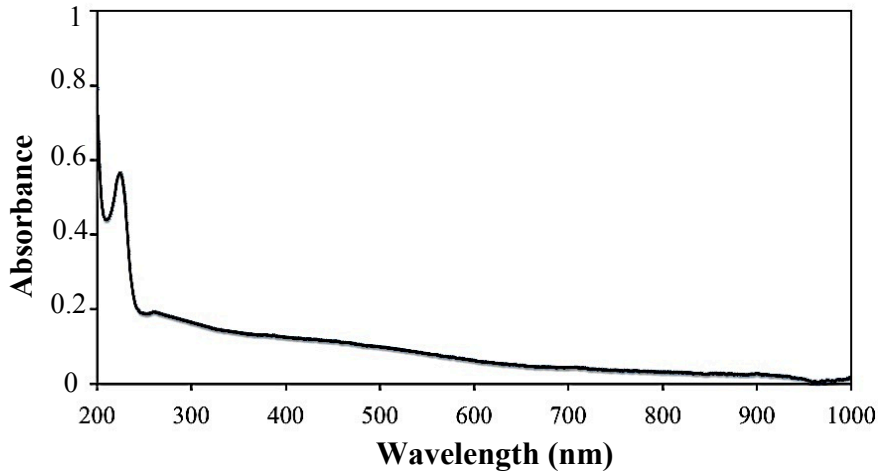

Figure 4.10. The UV-Vis absorption spectrum of 4CP with an absorbance peak at 225 nm.

The calibration curve of 4CP helps determine the concentration of the contaminant in an aqueous solution by correlating the absorbance values to the concentration considering the Beer-Lambert law (Eq.4.4) from which Eq.4.1 is derived.

$$A = \varepsilon c l \tag{4.4}$$

In Beer-Lambert's law A is the absorbance value, ε is the extinction coefficient, c is the concentration of the solute in the solution and l is the cell path length (the product of ε and c is the absorption coefficient α mentioned in Section 4.2.3). Fig.4.11 demonstrates the calibration curve of 4CP with the slope representing

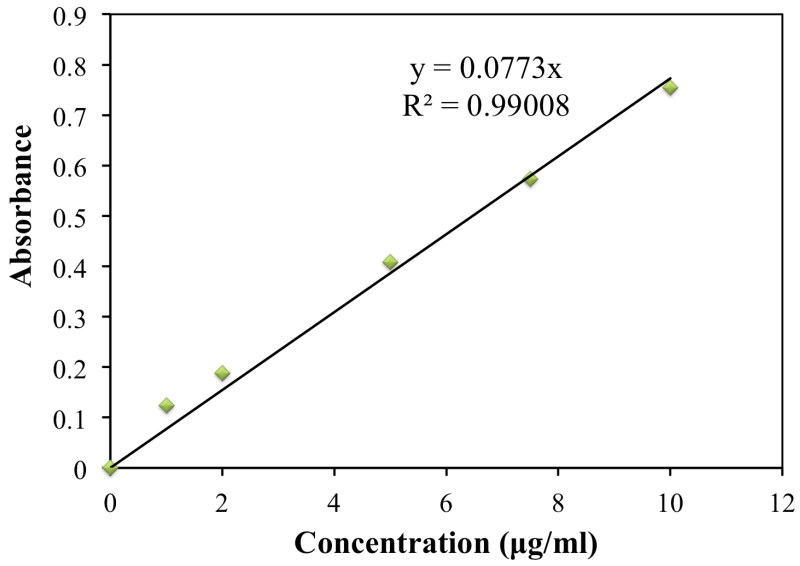

Figure 4.11. Calibration curve of 4CP demonstrating the linear correlation between the absorbance and the concentration of 4CP.

the extinction coefficient, given the fact that the cell path length is 1cm. The R squared value of over 0.99 for the fitted line deems the calibration curve valid.

4.4. Water Treatment

Fig.4.12 represents the relative change in the concentration of the contaminant 4CP in water for all 6 samples. The photocatalytic activity of the nanofibers is evident due to the fact that the reference sample 4CP-blank shows little signs of degradation over the testing period. This small change in the concentration is attributed to the direct photolysis caused by UV light since the reference sample 4CP-dark has demonstrated no change in concentration over the entire 360 min test duration. It has been established by Bertelli et al. that 2CP (2-Chlorophenol), another member of the chlorophenol family, is almost photostable in water under irradiation in the wavelength range of 315-400 nm; in the absence of any photocatalysts however, direct photolysis of this matter could happen under the irradiation in a much lower wavelength (254 nm) which is believed to be a direct consequence of C-Cl bond cleavage [85]. This is consistent with the data acquired from the UV light used in this study with an irradiation wavelength of 385 nm.

Fig.4.12 also implies that for samples 4CP-1 and 4CP-2 full degradation of the contaminant occurs in 90 min and 175 min respectively; in the case of 4CP-3 and 4CP-4 however, the declining change in contaminant concentration only continues up to 60 min and 120 min of UV irradiation, correspondingly.

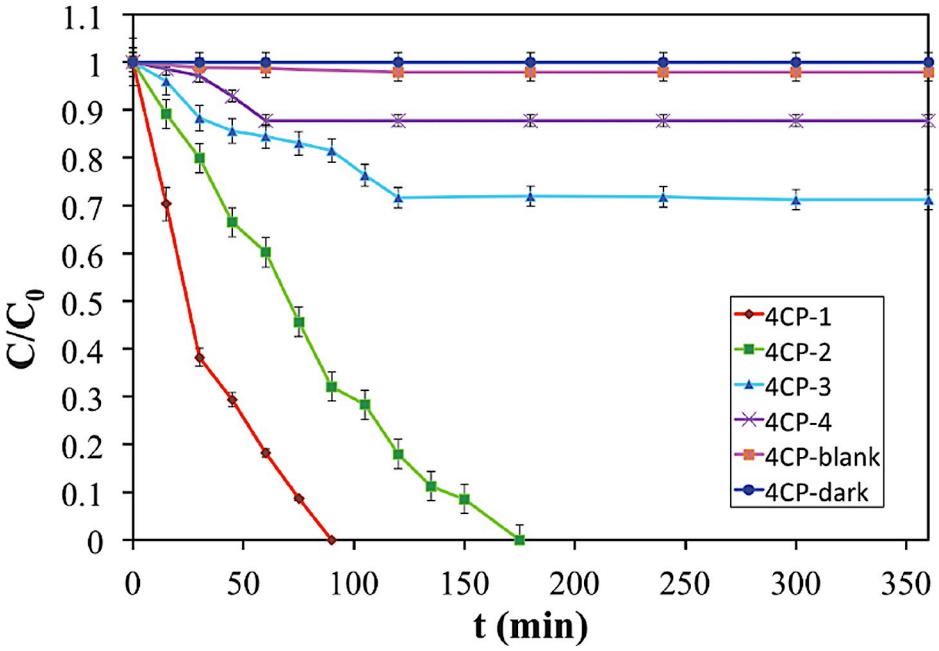

Figure 4.12. The degradation of 4CP in contact with BFO nanofibers as a result of irradiation by the light with the wavelength of 380nm. The gradual decrease in the different concentrations (1, 2, 5, 7.5 μg/ml) of 4CP compared to the insignificant change in concentration for 4CP-blank and 4CP-dark is depicted.

The halt in the photocatalytic activity of the nanofibers was speculated to be due to the saturation of the nanofiber surface by the relatively high concentration of the contaminant. To investigate this hypothesis, samples with an initial concentration of 5 μg/ml that were irradiated for 240 min (named as 4CP-sat) were removed from the system and the BFO nanofiber mats were rinsed with Milli-Q water. The mats were then returned to the solutions and UV irradiation was continued. As Fig.4.13 illustrates, the photocatalytic activity of the BFO was resumed after the nanofibers were rinsed and the degradation of 4CP-sat was

completed in an additional 180 min. This confirms the hypothesis of surface saturation of the nanofibers.

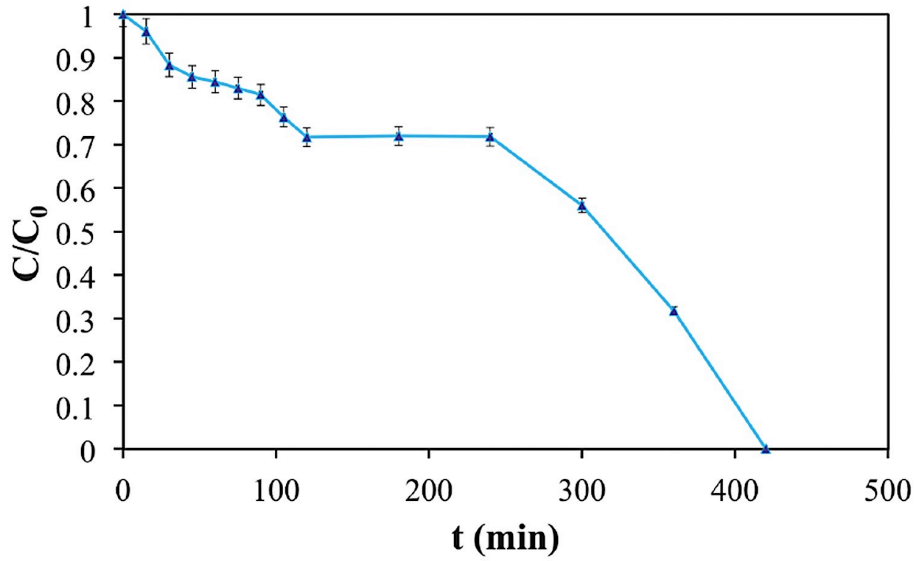

Figure 4.13. The degradation of 4CP for 4CP-sat sample; the trend shows a stop in the degradation process at 120 mins probably due to surface saturation and is resumed after the BFO nanofiber mat is rinsed.

The pH of the 4CP-sat sample was monitored throughout the testing period. The results indicated that the pH of the aqueous solution decreased with time (Fig.4.14). This decrease was attributed to the degradation of 4CP caused by the photocatalytic activity of BFO nanofibers since the change in the pH stopped in the duration in which the nanofiber mat was saturated, as shown in Fig4.13 and confirmed in Fig.4.14. The small change in the pH in the last hour of testing may be due to the small concentration of 4CP remaining in the solution as the degradation process approaches its end. The results show that after the photodegradation of the contaminant, it is recommended to add basic salts to

water in order to balance the pH back to a neutral value, taking into account that the added salts should not introduce new contaminants into the water.

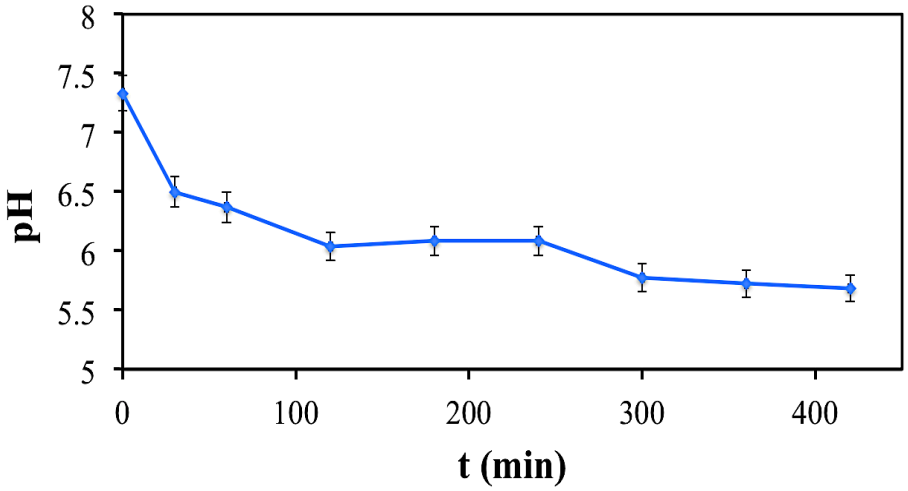

Figure 4.14. The changes in pH through the photodegradation of 4CP-sat.

In order to determine the governing kinetics of the degradation reactions of 4CP, the pseudo-first order model presented in Eq.3.1 was proposed. According to the nearly linear behavior of $ln(C/C_0)$ vs. t for 4CP-1, 4CP-2, 4CP-3 and 4CP-4 in their degradation period given in Fig.4.15 and R^2 values reported in Table 4.3, the suggested model fits the photodegradation data of 4CP in the presence of BFO nanofibers with close approximation.

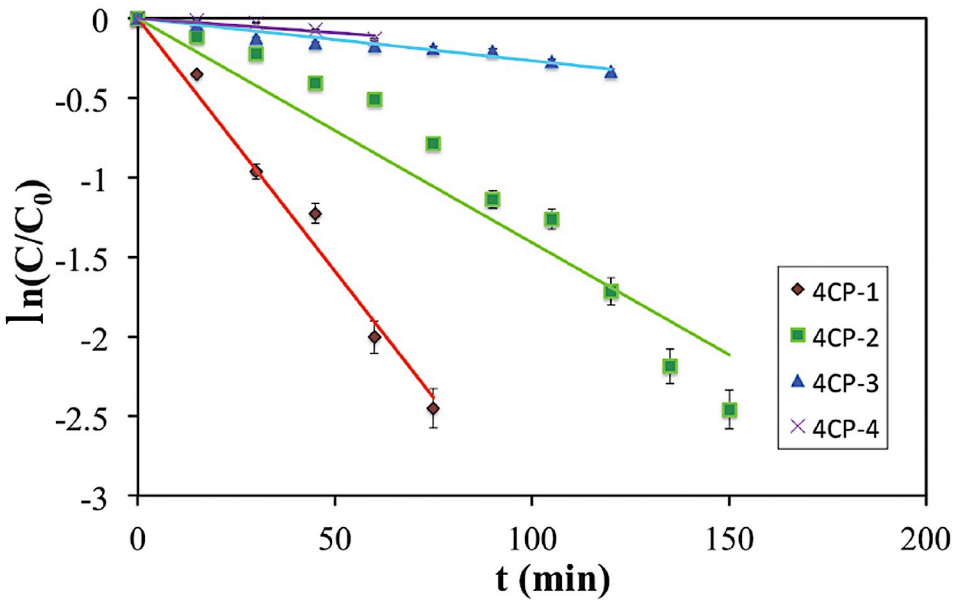

Figure 4.15. The application of pseudo-first order kinetics for the degradation of the 4CP.

Table 4.3 shows the reaction rate constant values calculated by applying the pseudo-first order model as well as the R^2 values of the linear fit. It could be hypothesized that the decrease in the reaction rate constant with the increase in the contaminant concentration is due to the higher amount of saturated sites on the surface of the BFO nanofibers at higher 4CP concentration. This decrease reduces the number of active sites where photocatalytic reactions occur [86].

Table 4.3. Kinetics parameters for 4CP degradation based on the pseudo-first order kinetics.

Samples	**k (min^{-1})**	**R^2**
4CP-1	-0.0317	0.9838
4CP-2	-0.014	0.9228
4CP-3	-0.0027	0.9416
4CP-4	-0.0018	0.8807

The results of deploying a 100 W light bulb to investigate the potential of using visible light to degrade 4CP are illustrated in Fig.4.16.

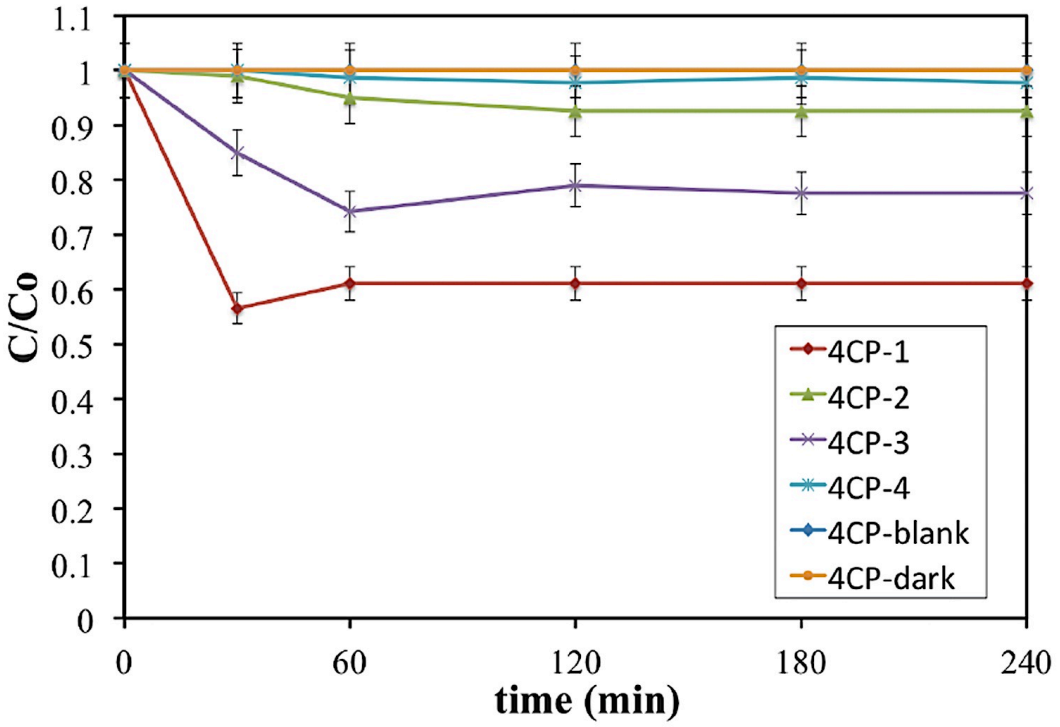

Figure 4.16. The degradation behavior of 4CP using visible light for samples 4CP-1, 4CP-2, 4CP-3, 4CP-4 and reference sample 4CP-blank; the changes in the concentration of 4CP through time in the 4CP-dark sample with no irradiation is also demonstrated which overlaps the 4CP-blank data.

By comparison, the degradation of 4CP by visible light as shown in Fig.4.16 is far less than what was observed for the same samples by UV irradiation (Fig.4.12); this is possibly due to the fact that the photons generated by the visible light of the light bulb did not provide sufficient energy for the photocatalysis process and most of the light produced was transformed into heat. Moreover, Fig.4.16 demonstrates that neither 4CP-blank nor 4CP-dark exhibited any change in concentration over the testing period; the stability of the contaminant in these

samples indicates that although the degradation of 4CP was less than in the case of UV irradiation, the degradation was in fact caused by photocatalysis with the assistance of BFO nanofibers. Furthermore, the wavelength range produced by the light bulb did not cause any direct photolysis of the contaminant since 4CP is photostable in this range. Further investigation is needed in order to understand the photocatalytic activity of BFO nanofibers in the visible range and the mechanism governing it.

4.5. BFO nanogrids

BFO nanogrids were fabricated with the aim to investigate the potential combination of the photocatalytic activity of the BFO nanofibers with the particulate removal ability of the nanogrids. Throughout all the parameter combinations tested, i.e., voltage, distance, motor speed and electrospinning process duration for each layer, the Nylon6 nanogrids were obtained by electrospinning with a voltage of 15 kV, a distance of 7.5 cm between the drum collector and nozzle, a rotating drum speed of 9000 rpm and finally 15 seconds of electrospinning for each layer before the target was rotated 90 °. Fig.4.17.a shows the SEM image of a Nylon6 nanogrid fabricated by this method with 4 layers of aligned nanofibers. For the purpose of comparison Fig.4.17.b and Fig.4.17.c show the SEM images of a Nylon6 nanogrid and a randomly oriented Nylon6 nanofiber mat obtained by conventional electrospinning, respectively.

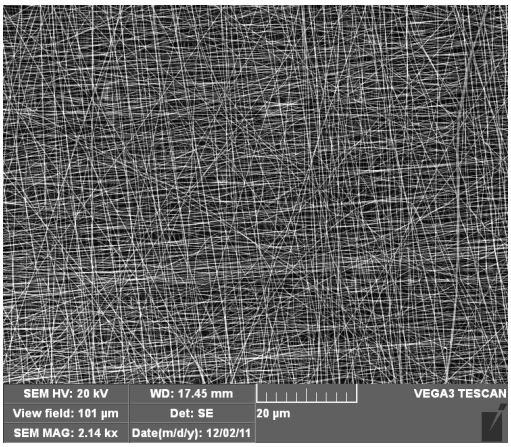

a

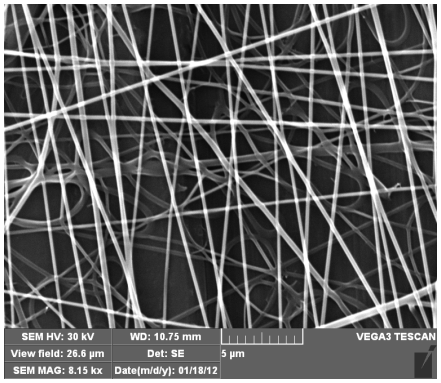

b

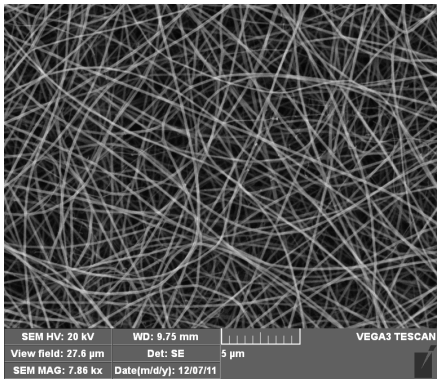

c

Figure 4.17. SEM images of a. Nylon6 nanogrid with 4 layers with a scale bar showing 20 µm; b. Nylon6 nanogrid at a higher magnification, c. randomly oriented Nylon6 nanofibers by conventional electrospinning. The scale bars represent 5 µm.

BFO nanogrids were electrospun through the same procedure mentioned above. The SEM images of the BFO/Nylon6 as spun nanogrid and BFO nanogrid after calcination at 600 °C are illustrated in Fig.4.18.a and Fig.4.18.b, respectively. The figure shows that the population of the nanofibers decreased after calcination,

since the Nylon6 surrounding the BFO was eliminated. The size of the nanofibers in average also decreased from 246 ± 65 nm to 122 ± 34 nm after calcination.

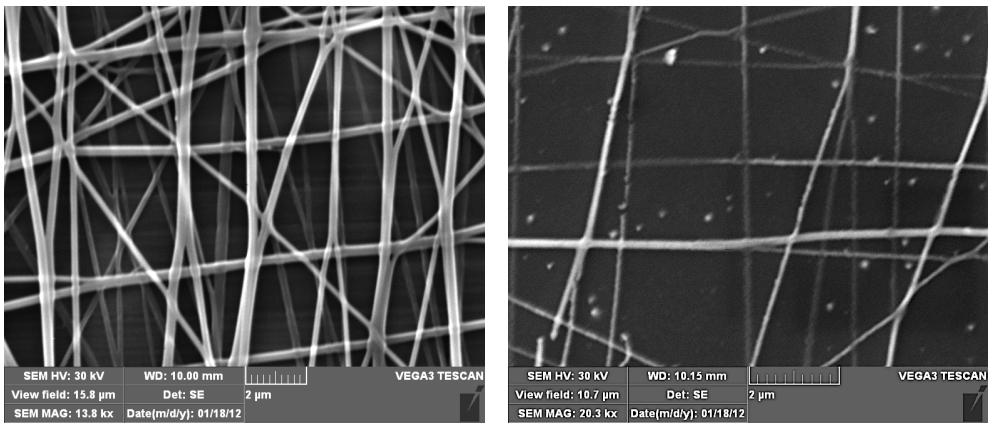

a b

Figure 4.18 SEM images of a. BFO/Nylon6 as spun nanogrid, b. BFO nanogrid after calcination at 600 °C; the scale bars show 2 µm.

In order to investigate the suitability of the BFO nanogrids for particulate filtration, the average size of the pores formed between the nanofibers were measured by SEM image analysis using 100 randomly chosen pores from each of the as-spun, dried and calcinated nanogrid samples. The results are summarized in Table 4.4.

Table 4.4. Pore size study of different nanogrid samples.

Nanogrid Sample	**Average pore size (µm^2)**	**Standard deviation (µm^2)**
As-spun BFO/Nylon6	8.47	4.84
Dried BFO/Nylon6	6.32	4.01
Calcinated BFO	2.90	1.61

The pore area sizes in Table.4.4 suggest that the BFO nanogrids are suitable candidates for particulate filtration, which can be combined with the photocatalytic activity of the nanofibers provided that the pore size area of the nanogrids does not exceed the particulate size. Moreover, as seen in Table.4.4, the average pore size of the nanogrids decreases after the drying stage and decreases even further after the calcination stage even though the standard deviation is fairly large. This decrease could be attributed to the decrease in the surface tension of the nanofibers with temperature that causes an overall shrinkage in the nanogrid size thus decreasing the nanogrid pore size. All in all, further investigation is needed to confirm these results and the suitability of BFO nanogrids in filtration applications.

Chapter 5: Conclusions and future works

In this chapter, conclusions made from this study are discussed. The conclusions section is then followed by the aspects of the study that have the capability to be pursued in the future.

5.1. Conclusions[1]

Producing nanofibers with controllable diameter and narrow size distribution is very important in many practical applications. We have investigated the effect of electric field and distance-voltage combination on the average diameter and size distribution of nanofibers of Nylon6 fabricated at room temperature by means of electrospinning of Nylon6 solution. SEM analysis of the electrospun fibers and diameter calculations indicate that the most proper electric field to obtain the finest fibers with the narrowest size distribution is E=1 kV/cm. We have found that even though maintaining the electric field at 1 kV/cm with a potential-distance combination of 7.5 kV-7.5 cm could result in the fabrication of the finest fibers, this voltage-distance combination results in a broad size distribution. A voltage-distance ratio of 15 kV-15 cm resulted in a narrow size distribution, although the average diameter was slightly larger than that obtained at 7.5 kV-7.5 cm field.

One-dimensional BFO nanofibers with an average fiber diameter of 130 ± 35 nm and average BFO crystallite size of 29 ± 2 nm were successfully fabricated through electrospinning and subsequent calcination at 600 °C. SEM images

[1] The procedure presented in this section has been published in the Journal of Scanning Microscopies, DOI 10.1002/sca.21044.

confirmed the formation of the Nylon6/BFO nanofibers prior to calcination and the continuous BFO nanofibers after high temperature calcination. Moreover, the band gap energy was calculated to be 2.5 eV.

The photocatalytic activity of BFO nanofibers was evident from the photodegradation of the pollutant 4-Chlorophenol under UV irradiation. The proposed pseudo-first order kinetics model deemed appropriate for the degradation of the contaminant. The results show promise for the application of BFO nanofibers in water purification due to a relatively low band gap energy that facilitates photoactivation; furthermore, the nanofiber structure holds the advantage of the elimination of the extra filtration stage of photocatalyst itself after the degradation process is complete [86].

5.2. Future Works

As shown in this study, there is promise for the application of BFO nanofiber mats in the photocatalytic degradation of water contaminants using visible light irradiation as well as UV light. Ergo, further study is necessary to explore the potential of BFO nanofibers in water treatment by exposure to visible light. In addition to that, preliminary study showed that the BFO nanogrids are potential candidates for particulate removal from water provided that the nanogrid pore area size does not exceed the size of the particulates; however, further study is required to confirm the potential application of the nanogrids in water treatment.

Bibliography

[1] J.F. Cooley, Patent GB 06385, Improved methods of and apparatus for electrically separating the relatively volatile liquid component from the component of relatively fixed substances of composite fluids (1900).

[2] J. F. Cooley, Patent US 692631, Apparatus for electrically dispersing fluids (1902).

[3] W. J. Morton, Patent US 705691, Method of dispersing fluids (1902).

[4] W. Gilbert, De Magnete, Dover publications (1991).

[5] A. Greiner and J. H. Wendorff, Electrospinning: A fascinating method for the preparation of ultrathin fibers, Angew. Chem. In. 46 (2007) 5670-5703.

[6] J. Doshi and D. H. Reneker, Electrospinning process and applications of electrospun fibers, J. Electrostat. 35 (1995) 151-160.

[7] V. G. Suvorov and E. A. Litvinov, Dynamic Taylor cone formation on liquid metal surface: numerical modeling, J. Phys. D. Appl. Phys. 33 (2000) 1245-1251.

[8] G. I. Taylor, Disintegration of water drops in an electric field, P. ROY. SOC. LOND. A. MAT. 280 (1964) 383-397.

[9] D. H. Reneker, A. L. Yarin, H. Fong and S. Koombhongse, Bending instability of electrically charged liquid jets of polymer solutions in electrospinning, J. Appl. Phys. 87 (2000) 4531-4547.

[10] F. Li, Y. Zhao and Y. Song, Core-Shell nanofibers: Nano channel and capsule by coaxial electrospinning, in: A. Kumar, Nanofibers, Intech publications (2010) 420-438.

[11] T. J. Sill and H A. von Recum, Electrospinning: applications in drug delivery and tissue engineering, Biomaterials 29 (2008) 1989-2006.

[12] S. K. Tiwari, R. Tzezana, E. Zussman and S. S. Venkatraman, Optimizing partition-controlled drug release from electrospun core–shell fibers, Int. J. Pharm. 392 (2010) 209-217.

[13] E. A. Buyuktanir, M. W. Frey and J. L. West, Self-assembled, optically responsive nematic liquid crystal/polymer core-shell fibers: Formation and characterization, Polymer 51 (2010) 4823-4830.

[14] Y. Su, Q. Su , W. Liu, M. Lim , J. R. Venugopal , X. Mo, S. Ramakrishna, S. S. Al-Deyab and M. El-Newehy, Controlled release of bone morphogenetic

protein 2 and dexamethasone loaded in core–shell PLLACL–collagen fibers for use in bone tissue engineering, Acta Biomater. 8 (2012) 763-771.

[15] S. L. Quan, H. S. Lee, E. H. Lee, K. D. Park, S. Gol Lee and I. J. Chin, Ultrafine PMMA(QDs)/PVDF core–shell fibers for nanophotonic applications, Microelectron. Eng. 87 (2010) 1308-1311.

[16] Y. Kong, J. Yuan and J. Qiu, Preparation and characterization of aligned carbon nanotubes/polylactic acid composite fibers, Physica B 407 (2012) 2451-2457.

[17] A. Cooper, N. Bhattarai1 and M. Zhang, Fabrication and cellular compatibility of aligned chitosan–PCL fibers for nerve tissue regeneration, Carbohyd. Polym. 85 (2011) 149-156.

[18] H. B.Wang, M. E. Mullins, J. M. Cregg, A. Hurtado, M. Oudega, M. T. Trombley and R. J. Gilbert, Creation of highly aligned electrospun poly-L-lactic acid fibers for nerve regeneration applications, J. Neural Eng. 6 (2009) 016001.

[19] Y. Yang, X. Li , M. Qi, S. Zhou and J.Weng, Release pattern and structural integrity of lysozyme encapsulated in core–sheath structured poly(DL-lactide) ultrafine fibers prepared by emulsion electrospinning, Eur. J. Pharm. Biopharm. 69 (2008) 106-116.

[20] X. Xu, X. Chen, P. Ma, X. Wang and X. Jing, The release behavior of doxorubicin hydrochloride from medicated fibers prepared by emulsion-electrospinning, Eur. J. Pharm. Biopharm. 70 (2008) 165-170.

[21] R.C Pullar, S.G Appleton, M.H Stacey, M.D Taylor and A.K Bhattacharya, The manufacture and characterisation of aligned fibres of the ferroxplana ferrites Co-Z, 0.67% CaO-doped Co-Z, Co-Y and Co-W, J. Magn. Magn. Mater. 186 (1998) 313-325.

[22] P. D. Dalton, D. Grafahrend, K. Klinkhammer, D. Klee and M. Möller, Electrospinning of polymer melts: Phenomenological observations, Polymer 48 (2007) 6823-6833.

[23] H. H. Huang, C. L. He, H. S.Wang and X. M. Mo, Preparation of core-shell biodegradable microfibers for long-term drug delivery, J. Biomed. Mater. Res. A 90 (2009) 1243-1251.

[24] Polymer Scaffold Fabrication, M. B. Murphy and A G. Mikos, in: R. Lanza, R. Langer and J. Vacanti, Principles of Tissue Engineering, Academic press, (2007) 309-321.

[25] W. J. Lia, R. L. Mauck, J. A. Cooper, X. Yuana and R. S. Tuan, Engineering controllable anisotropy in electrospun biodegradable nanofibrous scaffolds for musculoskeletal tissue engineering, J. Biomech. 40 (2007) 1686-1693.

[26] Q. Lin, Y. Li and M. Yang, Polyaniline nanofiber humidity sensor prepared by electrospinning, Sens. Actuators. B. Chem. 161 (2012) 967-972.

[27] H. Du, J. Wang, M. Su, P. Yao, Y. Zheng and N. Yu, Formaldehyde gas sensor based on SnO_2/In_2O_3 hetero-nanofibers by a modified double jets electrospinning process, Sens. Actuators. B. Chem. 166-167 (2012) 746-752.

[28] X. Song, D. Zhang and M. Fan, A novel toluene sensor based on ZnO–SnO_2 nanofiber web, Appl. Surf. Sci. 255 (2009) 7343-7347.

[29] Y. Xiu-Yun, X. Chun-Ying, Y. Bai-Qing and Y. Tian-Yan, A Novel Electrochemiluminescence Electrospun Carbon Nanofiber Based Sensor for Atropine, Chinese J. Anal. Chem. 39 (2011) 1233-1237.

[30] M. Z. Ongun, K. Ertekin, M. Gocmenturk, Y. Ergun and A. Suslu, Copper ion sensing with fluorescent electrospun nanofibers, Spectrochim. ACTA. A. 90 (2012) 177-185.

[31] S. Kacmaz, K. Ertekin, A. Suslu, M. Ozdemir, Y. Ergun, E. Celik and U. Cocen, Emission based sub-nanomolar silver sensing with electrospun nanofibers, Sens. Actuators. B. Chem. 153 (2011) 205-213.

[32] A.M. Bazargan, M. Keyanpour-rad, F.A. Hesari, M. Esmaeilpour Ganji, A study on the microfiltration behavior of self-supporting electrospun nanofibrous membrane in water using an optical particle counter, Desalination 265 (2011) 148-152.

[33] R. Gopal, S. Kaur, Z. Ma, C. Chan, S. Ramakrishna, T. Matsuura, Electrospun nanofibrous filtration membrane, J. Membrane Sci. 281 (2006) 581-586.

[34] N. Savage and M. S. Diallo, Nanomaterials and water purification: Opportunities and challenges, J. Nanopart. Res. 7 (2005) 331-342.

[35] W. Q. Betancourt and J. B. Rose, Drinking water treatment processes for removal of Cryptosporidium and Giardia, Vet. Parasitol. 126 (2004) 219-234.

[36] B. Van der Bruggena, M. Mänttäri and M. Nyström, Drawbacks of applying nanofiltration and how to avoid them: A review, Sep. Purif. Technol. 63 (2008) 251-263.

[37] B. Van der Bruggen and C. Vandecasteele, Removal of pollutants from surface water and groundwater by nanofiltration: overview of possible applications in the drinking water industry, Environ. Pollut. 122 (2003) 435-445.

[38] Z. Ma, H. Ji, Y. Teng , G. Dong, J. Zhou , D. Tan and J. Qiu, Engineering and optimization of nano- and mesoporous silica fibers using sol–gel and electrospinning techniques for sorption of heavy metal ions, J. Colloid. Interf.

SCI. 358 (2011) 547-553.

[39] W. J. Weber, Adsorption processes, University of Michigan, retrieved from: http://pac.iupac.org/publications/pac/pdf/1974/pdf/3703x0375.pdf.

[40] P. Huck and M. Sozański, Chemical basis for water technology, in: Peter Wilderer, Treatise on Water Science, Vol.3: Aquatic Chemistry and Biology (2011) 429-469.

[41] F. G. Helfferich, Ion Exchange, Courier Dover publications (1995) 15.

[42] S. Esplugas, J. Giménez, S. Contreras, E. Pascual and M. Rodríguez, Comparison of different advanced oxidation processes for phenol degradation, Water Res. 36 (2002) 1034-1042.

[43] D. Khomskii. Classifying multiferroics: mechanisms and effects, Physics 2 (2009) 20.

[44] A.Z. Simões, R.F. Pianno, E.C. Aguiar, E. Longo, J.A. Varela, Effect of niobium dopant on fatigue characteristics of $BiFeO_3$ thin films grown on Pt electrodes, J. Alloys. Compd. 479 (2009) 274–279.

[45] T. Han, D. H. Reneker and A. L. Yarin, Buckling of jets in electrospinning, Polymer 48 (2007) 6064-6076.

[46] S. K. Tiwari and Subbu S. Venkatraman, Importance of viscosity parameters in electrospinning: Of monolithic and core–shell fibers, Mater. Sci. Eng. C 32 (2012) 1037-1042.

[47] S.A. Theron, E. Zussmana, A.L.. Yarin, Experimental investigation of the governing parameters in the electrospinning of polymer solutions, Polymer 45 (2004) 2017-2030.

[48] M. Bognitzki, W. Czado, T. Frese, A. Schaper, M. Hellwig, M. Steinhart, A. Greiner, and J. H. Wendorff, Nanostructured fibers via wlectrospinning, Adv. Mater. 13 (2001) 70-72.

[49] S. S. Ojha, M. Afshari, R. Kotek and R. E. Gorga, Morphology of electrospun Nylon-6 nanofibers as a function of molecular weight and processing parameters, J. Appl. Polym. Sci. 108 (2008) 308-319.

[50] C.J. Thompson, G.G. Chase, A.L. Yarin , D.H. Reneker, Effects of parameters on nanofiber diameter determined from electrospinning model, Polymer 48 (2007) 6913-6922.

[51] O.S. Yördem, M. Papila and Y.Z. Menceloğlu, Effects of electrospinning parameters on polyacrylonitrile nanofiber diameter: An investigation by response surface methodology, Mater. Design 29 (2008) 34-44.

[52] V. Pornsopone, P. Supaphol, R. Rangkupan and S. Tantayanon, Electrospinning of methacrylate-based copolymers: Effects of solution concentration and applied electrical potential on morphological appearance of as-spun fibers, Polym. Eng. Sci. 45 (2005) 1073-1080.

[53] S.Y. Gu, J. Ren and G.J. Vancso, Process optimization and empirical modeling for electrospun polyacrylonitrile (PAN) nanofiber precursor of carbon nanofibers, Eur. Polym. J. 41 (2005) 2559-2568.

[54] J. S. Lee, K. H. Choi, H. D. Ghim, S. S. Kim, D. H. Chun, H. Y. Kim and W. S. Lyoo, Role of molecular weight of atactic poly (vinyl alcohol) (PVA) in the structure and properties of PVA nanofabric prepared by electrospinning, J. Appl. Polym. SCI. 93 (2004) 1638-1646.

[55] L. Li, Y. L. Hsieh, Ultra-fine polyelectrolyte fibers from electrospinning of poly (acrylic acid), Polymer 46 (2005) 5133-5139.

[56] H. Homayoni, S. A. Hosseini Ravandi, M. Valizadeh, Electrospinning of chitosan nanofibers: Processing optimization, Carbohyd. Polym. 77 (2009) 656-661.

[57] S. Sukigara, M. Gandhi, J. Ayutsede, M. Micklusc and F. Ko, Regeneration of Bombyx mori silk by electrospinning. Part 2. Process optimization and empirical modeling using response surface methodology, Polymer (45) pp. 3701-3708.

[58] P. Heikkilä and A. Harlin, Parameter study of electrospinning of polyamide-6, Eur. Polym. J. 44 (2008) 3067–3079.

[59] J.M. Deitzel, J. Kleinmeyer, D. Harris, N.C. Beck Tan, The effect of processing variables on the morphology of electrospun nanofibers and textiles, Polymer, 42 (2001) 261-272.

[60] V. Beachley and X. Wen, Effect of electrospinning parameters on the nanofiber diameter and length, Mat. Sci. Eng. C 29 (2009) 663-668.

[61] D. Y. Lee, B. Y. Kim, S. J. Lee, M. H. Lee, Y. S. Song and J. Y. Lee, Titania Nanofibers Prepared by Electrospinning, J. Korean Phys. Soc. 48 (2006) 1686-1690.

[62] N. Keller, G. Rebmann, E. Barraud, O. Zahraa, V.Keller, Macroscopic carbon nanofibers for use as photocatalyst support, Catal. Today 101 (2005) 323-329.

[63] J. Herrmann, Heterogeneous photocatalysis: fundamentals and applications to the removal of various types of aqueous pollutants, Catal. Today 53 (1999) 115-129.

[64] H. C. Liang, X. Z. Li, Y. H. Yang and K. Hung Sze, Comparison of the degradations of diphenamid by homogeneous photolysis and heterogeneous photocatalysis in aqueous solution, Chemosphere 80 (2010) 366-374.

[65] V. Augugliaro, M. Litter, L. Palmisano and J. Soria, The combination of heterogeneous photocatalysis with chemical and physical operations: A tool for improving the photoprocess performance, Journal of Photochemistry and Photobiology C: Photochemistry Reviews 7 (2006) 127-144.

[66] M. N. Chong, B. Jin, C. W.K. Chow and C. Saint, Recent developments in photocatalytic water treatment technology: A review, Water Res. 44 (2010) 2997-3027.

[67] L. Liu, Z. Liu, H. Bai and D. D. Sun, Concurrent filtration and solar photocatalytic disinfection/degradation using high-performance Ag/TiO_2 nanofiber membrane, Water Res. 46 (2012) 1101 -1112.

[68] M. S. Lee, S. S. Park, G. Lee, C. Ju, S. Hong, Synthesis of TiO_2 particles by reverse microemulsion method using nonionic surfactants with different hydrophilic and hydrophobic group and their photocatalytic activity, Catal. Today 101 (2005) 283-290.

[69] M. Hussain, R. Ceccarelli, D.L. Marchisio, D. Fino, N. Russo, F. Geobaldo, Synthesis, characterization, and photocatalytic application of novel TiO_2 nanoparticles, Chem. Eng. J. 157 (2010) 45-51.

[70] X.H. Xia, Y. Liang, Z. Wang, J. Fan, Y.S. Luo, Z.J. Jia, Synthesis and photocatalytic properties of TiO_2 nanostructure, Mater. Res. Bull. 43 (2008) 2187-2195.

[71] G. Laera, B. Jin, H. Zhu, A. Lopez, Photocatalytic activity of TiO_2 nanofibers in simulated and real municipal effluents, Catal. Today 161 (2011) 147-152.

[72] Z. Liu, X. Zhang, S. Nishimoto, T. Murakami, AND A. Fujishima Efficient Photocatalytic Degradation of Gaseous Acetaldehyde by Highly Ordered TiO_2 Nanotube Arrays, Environ. Sci. Technol. 42 (2008) 8547-8551.

[73] K. Sunada, Y. Kikuchi, K. Hashimoto and A. Fujishima, Bactericidal and Detoxification Effects of TiO_2 Thin Film Photocatalysts, Environ. Sci. Technol. 32 (1998) 726-728.

[74] H. Choi, E. Stathatos and D. D. Dionysiou, Photocatalytic TiO_2 films and membranes for the development of efficient wastewater treatment and reuse systems, Desalination 202 (2007) 199-206.

[75] S. K. Choi, S. Kim, S. K. Lim, and H. Park, Photocatalytic comparison of TiO2 nanoparticles and electrospun TiO_2 nanofibers: effects of mesoporosity and interparticle charge transfer, J. Phys. Chem. C 114 (2010) 16475-16480.

[76] J. F. Ihlefeld, N. J. Podraza, Z. K. Liu, R. C. Rai, X. Xu, T. Heeg, Y. B. Chen, J. Li, R. W. Collins, J. L. Musfeldt, X. Q. Pan, J. Schubert, R. Ramesh and D. G. Schlom, Optical band gap of $BiFeO_3$ grown by molecular-beam epitaxy, Appl. Phys. Lett. 92 (2008) 142908-1-142908-3.

[77] A. J. Hauser, J. Zhang, L. Mier, R. A. Ricciardo, P. M. Woodward, T. L. Gustafson, L. J. Brillson, and F. Y. Yang, Characterization of electronic structure and defect states of thin epitaxial $BiFeO_3$ films by UV-Visible absorption and cathodoluminescence spectroscopies, Appl. Phys. Lett. 92 (2008) 222901-1-222901-3.

[78] S. Li, Y. H. Lin, B. P. Zhang, C. W. Nan, and Y. Wang, Photocatalytic and magnetic behaviors observed in nanostructured $BiFeO_3$ particles, J. Appl. Phys. 105 (2009) 056105-1-056105-3.

[79] X. Xu, Y. H. Lin, P. Li, L. Shu, and C. W. Nan, Synthesis and photocatalytic behaviors of high surface area $BiFeO_3$ thin films, Journal of American Ceramics Society 94 (2011) 2296–2299.

[80] F. Gao, X. Chen, K. Yin, S.Dong, Z. Ren, F.Yuan, T. Yu, Z. Zou, and J.M. Liu, Visible-Light photocatalytic properties of weak magnetic $BiFeO_3$ nanoparticles, Adv. Mater. 19 (2007) 2889–2892.

[81] E. Leyva, E. Moctezuma, M.G. RuõÂz, L. Torres-MartõÂnez, Photodegradation of phenol and 4-chlorophenol by $BaO\text{-}Li_2O\text{-}TiO_2$ catalysts, Catal. Today 40 (1998) 367-376.

[82] H. S. Son, S. J. Lee, I. H. Cho, K. D. Zoh , Kinetics and mechanism of TNT degradation in TiO_2 photocatalysis, Chemosphere 57 (2004) 309-317.

[83] L. Yang, M. Guiping, F. Dawei, X. Juan, Z. Hongwen, Effects of solution properties and electric field on the electrospinning of hyaluronic acid, Carbohyd. Polym. 83 (2011) 1011-1015.

[84] N. Shakti, P.S.Gupta, Structural and optical properties of sol-gel prepared ZnO thin film, Applied Physics Research 1(2) (2010) 19-28.

[85] M. Bertelli, E. Selli, Reaction paths and efficiency of photocatalysis on TiO_2 and of H2O2 photolysis in the degradation of 2-chlorophenol, J. Hazard. Mater. B 138 (2006) 46-52.

[86] I. Poulios, I. Tsachpinis, Photodegradation of the textile dye Reactive Black 5 in the presence of semiconducting oxides. J. Chem. Technol. Biot. 74 (1999) 349-357.